Stratospheric Influences on the MJO-Induced Rossby Wave Train: Effects on Intraseasonal Climate

LON L. HOOD

Lunar and Planetary Laboratory, The University of Arizona, Tucson, Arizona

MALORI A. REDMAN

Department of Earth and Climate Science, San Francisco State University, San Francisco, California

WES L. JOHNSON

Lunar and Planetary Laboratory, The University of Arizona, Tucson, Arizona

THOMAS J. GALARNEAU JR.

Cooperative Institute for Mesoscale Meteorological Studies, University of Oklahoma, and NOAA/OAR/National Severe Storms Laboratory, Norman, Oklahoma

ABSTRACT

The tropical Madden–Julian oscillation (MJO) excites a northward propagating Rossby wave train that largely determines the extratropical surface weather consequences of the MJO. Previous work has demonstrated a significant influence of the tropospheric El Niño–Southern Oscillation (ENSO) on the characteristics of this wave train. Here, composite analyses of ERA-Interim sea level pressure (SLP) and surface air temperature (SAT) data during the extended northern winter season are performed to investigate the additional role of stratospheric forcings [the quasi-biennial oscillation (QBO) and the 11-yr solar cycle] in modifying the wave train and its consequences. MJO phase composites of 20–100-day filtered data for the two QBO phases show that, similar to the cool phase of ENSO, the easterly phase of the QBO (QBOE) produces a stronger wave train and associated modulation of SLP and SAT anomalies. In particular, during MJO phases 5–7, positive SLP and negative SAT anomalies in the North Atlantic/Eurasian sector are enhanced during QBOE relative to the westerly phase of the QBO (QBOW). The opposite occurs during the earliest MJO phases. SAT anomalies over eastern North America are also more strongly modulated during QBOE. Although less certain because of the short data record, there is some evidence that the minimum phase of the solar cycle (SMIN) produces a similar increased modulation of SLP and SAT anomalies. The strongest modulations of SLP and SAT anomalies are produced when two or more of the forcings are superposed (e.g., QBOE/cool ENSO, SMIN/QBOE, etc.).

1. Introduction

The 30–60-day Madden–Julian oscillation (MJO) is an eastward-propagating pattern of alternately intense and weak tropical convection and precipitation primarily in the Indo-Pacific region (Madden and Julian 1971, 1972).

It is the dominant mode of tropical intraseasonal climate variability (e.g., Zhang 2013). The MJO can be divided into eight phases defined such that phases 1–3 correspond to convection over Africa and the Indian Ocean, phases 4 and 5 to convection over the Maritime Continent, and phases 6–8 to convection in the western Pacific and date line region (Wheeler and Hendon 2004; Kiladis et al. 2014). Diabatic heating anomalies caused by the MJO excite global-scale Rossby wave trains (characterized by alternately high and low sea level pressure or geopotential height anomalies) emanating especially from the tropical warm pool region centered on the Maritime

Continent. These wave trains propagate across Southeast Asia, the North Pacific, North America, the Atlantic, and the Southern Hemisphere (Matthews et al. 2004), projecting onto the Pacific–North American (PNA) and North Atlantic Oscillation (NAO) patterns (Ferranti et al. 1990; Scaife et al. 2017). The latter "teleconnection" patterns account for a major fraction of intraseasonal circulation variance at mid- to high latitudes during boreal winter (Wallace and Gutzler 1981).

A review of tropical–extratropical interactions on intraseasonal time scales, including effects of MJO teleconnections, has been given by Stan et al. (2017). As discussed there, MJO teleconnections have been found to affect variations of the Northern Hemisphere storm track and extratropical cyclone activity (e.g., Guo et al. 2017), the occurrence and location of "atmospheric river" precipitation events along the west coast of North America (e.g., Baggett et al. 2017), and the occurrence of winter blocking episodes, which can lead to extreme weather events (Hamill and Kiladis 2014; Henderson et al. 2016). Effects of the MJO-induced Rossby wave train on temperature and precipitation over the continental United States have been documented by Bond and Vecchi (2003) and Zhou et al. (2012). In the Atlantic/European region, the daily wintertime NAO index, defined approximately as the sea level pressure over Portugal minus that over Iceland, tends to be negative or neutral during the earliest MJO phases but becomes positive on average within 10–15 days after the occurrence of MJO phase 3 (Cassou 2008; Lin et al. 2009).

In addition to evidence for stratospheric influences on the MJO, which is the main topic of this paper, there is evidence for MJO influences on the stratosphere, which can have secondary effects on tropospheric intraseasonal climate. Specifically, the upward propagation of an enhanced Rossby wave train during strong boreal winter MJO events can assist in breaking down the stratospheric polar vortex, leading to the occurrence of sudden stratospheric warmings (SSWs) (Garfinkel et al. 2012, 2014). SSWs, in turn, produce a downward propagating zonal wind anomaly that favors a negative phase of the northern annular mode or Arctic Oscillation, a close cousin of the NAO (Baldwin and Dunkerton 2001; Polvani and Waugh 2004). For example, an especially strong MJO event in February 2018 was followed by a major SSW (e.g., Butler et al. 2018; Pawson et al. 2018) and a negative phase of the NAO that has been associated with a severe cold period in Europe at the end of that month (Kodera et al. 2018).

In this paper, an effort is made to evaluate the importance of several forms of tropospheric and stratospheric forcings for influencing the overall occurrence rate and extratropical consequences of strong MJO events during the extended boreal winter season [November–April

(NDJFMA)]. Although some previous studies, summarized below, have evaluated the effects of the tropospheric El Niño–Southern Oscillation (ENSO) and the stratospheric quasi-biennial oscillation (QBO) on specific aspects of MJO-induced extratropical circulation anomalies (e.g., North Pacific storm track activity and atmospheric river events), a broader approach is taken here. In particular, the extent to which these forcings, whether individually or in combination, affect the overall activity of the MJO itself, the strength and geographic evolution of the MJO-induced Rossby wave train, and the resulting amplitudes of intraseasonal surface air temperature anomalies, is examined. In addition to the QBO, the contribution of 11-yr solar forcing of the stratosphere [the quasi-decadal oscillation (QDO)] is investigated. For this purpose, a calculation of normalized occurrence rates of strong MJO events for the different phases of ENSO, the QBO, and the QDO is first carried out. Then, compositing analyses are performed of ERA-Interim reanalysis daily sea level pressure (SLP) and 2-m surface air temperature (SAT) data as a function of MJO phase in boreal winter over a 38-yr period (1979–2016).

In section 2, the datasets and methodology are described. In section 3, the normalized occurrence rates are calculated. In section 4, the mean NDJFMA MJO modulations of SLP and SAT and their interpretation are reviewed. As will be seen, especially large MJO modulations of mean SLP and SAT anomalies are produced in both the North Pacific and North Atlantic/ Eurasian sectors. To allow a more quantitative analysis, several concise diagnostics of the overall strength of the wave train and the modulation of SLP and SAT anomalies in the North Atlantic/Eurasian sector are defined. In section 5, the changes in the wave train amplitude and the MJO modulation that occur during the separate phases of ENSO are determined for comparison to previous work. In section 6, the changes in the MJO modulation that occur during the separate phases of the QBO are determined. Similarities between the QBOE (QBOW) changes and those that occur under cool (warm) ENSO conditions are noted, where QBOE is the easterly phase of the QBO and QBOW the westerly phase. The SLP and SAT diagnostics introduced in section 4 are then applied to investigate how the QBO influence on the wave train and SAT anomalies depends on the phase of ENSO (e.g., QBOE/cool ENSO vs QBOW/warm ENSO conditions). Spatial correlations are also calculated to quantify the similarities between the QBO and ENSO compositing results. In section 7, the MJO modulation calculation is repeated for the two phases of the QDO (SMIN and SMAX, the minimum and maximum phases of the solar cycle). Similarities between the SMIN changes and those that occur under cool ENSO and easterly QBO conditions

are again noted. This leads to further applications of the SLP and SAT diagnostics to investigate changes in the MJO modulation under SMIN/QBOE, SMAX/QBOW, SMIN/cool ENSO, and SMAX/warm ENSO conditions. A discussion of the overall results, possible mechanisms, and suggestions for future work are given in section 8.

2. Datasets and methodology

With the exception of the SLP and SAT data, all of the daily data needed for compositing and calculation of normalized occurrence rates (i.e., MJO, ENSO, QBO, and QDO indices) have been described in detail in section 3 of Hood (2018; Fig. 2 therein plots most of these data).

Briefly, to determine the amplitude and phase of the MJO on a given day, the outgoing longwave radiation (OLR)-based MJO index (OMI) of Kiladis et al. (2014) is adopted. The OMI data are available from the NOAA Earth System Research Laboratory (http://www.esrl.noaa.gov/psd/mjo/mjoindex). The index consists of a projection of 20–96-day filtered satellite OLR data onto the daily spatial empirical orthogonal function (EOF) patterns of 30–96-day eastward-filtered OLR. The daily OMI amplitude is the square root of the sum of squares of the daily eigenvalues of the first two EOFs. The OMI is normalized so that an amplitude of 1.0 corresponds to one standard deviation. The daily MJO phase can also be calculated from these two daily eigenvalues as formulated originally by Wheeler and Hendon (2004) for the alternate Real-time Multivariate MJO (RMM) index. OMI amplitudes of at least 1.0 are normally considered to be a minimum for a significant MJO event. However, as discussed in section 4, in order to increase the detectability of ENSO and stratospheric influences on the MJO modulation of extratropical circulation, it is helpful to restrict analyses to days when stronger MJO events with OMI amplitudes >1.5 are in progress.

As an indicator of the phase of ENSO, the Niño-3.4 index (N3.4), which is defined as the mean sea surface temperature anomaly within 5°S–5°N, 120°–170°W, is adopted. Daily values of N3.4 are available from http://www.cpc.ncep.noaa.gov/data/indices. For simplicity and to provide as many days as possible for the MJO phase composites, most analyses are done with cool (warm) ENSO conditions defined as N3.4 < 0 (>0). However, for comparison purposes, additional analyses are also performed in section 5 for more active ENSO conditions, accepting only days with N3.4 < −1 K or N3.4 > 1 K. This differs somewhat from the work of Moon et al. (2011), who considered 15 contiguous DJF winters when N3.4 was either strongly positive or negative for the entire winter, representing true El Niño or La Niña

conditions. It also differs from the work of Nishimoto and Yoden (2017), who considered cool (warm) ENSO conditions to exist when N3.4 was < −1 K (> 1 K). Nevertheless, as will be seen in section 5, clear differences between the two ENSO composites are obtained even if the simple definition is used.

As an index of QBO variability, most previous studies have used equatorial winds at levels ranging from 40 to 50 hPa (e.g., Baldwin et al. 2001). Here, we use equatorial winds at 50 hPa (u50) to be consistent with previous studies (e.g., Yoo and Son 2016; Hood 2017). However, both the normalized occurrence rates calculated in section 3 and the compositing results presented in sections 6 and 7 change in only minor ways if 40 or 45 hPa is chosen as the monitoring level. Monthly mean equatorial values of u50 based on radiosonde data are available from the Freie Universität Berlin (http://www.geo.fu-berlin.de/en/met/ag/strat/produkte/qbo/index.html). Daily values in a given month are assumed to be equal to the monthly means. Again for simplicity and to maximize the number of composited days, most analyses are done with westerly (easterly) QBO defined as u50 > 0 (<0). However, for comparison, alternate analyses are performed in section 6 for "more active westerly (easterly)" conditions, defined as u50 > 5 m s^{-1} (< −10 m s^{-1}).

Finally, as a measure of solar UV variability, the solar flux at 205 nm (F205), estimated according to the Naval Research Laboratory model, version 2 (NRL2; e.g., Lean 2000) is adopted. Daily NRL2 F205 data are available from the Laboratory for Atmospheric and Space Physics at the University of Colorado (http://lasp.colorado.edu/lisird/data/nrl2_files). F205 is used because it is a direct measure of solar forcing of the upper stratosphere that leads to a tropical lower stratospheric dynamical response (section 7). It correlates closely with a variety of more familiar solar phenomena including sunspot number and solar flare occurrence. As seen in Fig. 2 of Hood (2018), the three full solar cycles during 1979–2016 varied in length from ∼10 to ∼12 years. The most recent solar maximum in ∼2014 was reduced in amplitude compared to the previous three maxima, possibly indicating an approaching minimum in the 70–100-yr Gleissberg cycle (e.g., Peristykh and Damon 2003).

The two phases of the QDO (SMAX and SMIN) were assumed to exist when the daily value of F205 was ≥10.5 or ≤10.1 mW m^{-2} nm^{-1}, respectively. These restrictive limits (accepting only strongly maximum or minimum conditions) were chosen both to maximize the solar signal and to avoid most of the periods when the tropical lower stratosphere was affected by volcanic aerosol injections. However, the 1982/83 winter following El Chichón and the 1991/92 winter following Pinatubo when aerosol heating of the tropical lower stratosphere

was significant remains in the SMAX category. Therefore, tests of whether the occurrence rate and compositing results for SMAX conditions could be affected by volcanic aliasing are carried out as discussed in sections 3 and 7.

To determine daily values of sea level pressure (SLP) and 2-m surface air temperature (SAT), the European Centre for Medium-Range Weather Forecasts interim reanalysis (ERA-Interim) dataset (Dee et al. 2011) is employed over the 1979–2016 period. Four times daily SLP and SAT data were first downloaded in monthly increments from http://apps.ecmwf.int/datasets on a $1° \times 1°$ grid. Daily averages were then calculated and interpolated to a $3° \times 3°$ grid. At a given grid point, the seasonal cycle was minimized by subtracting the long-term monthly mean of either SLP or SAT from each daily mean.

To extract the intraseasonal component of variability, a 20- to 100-day Lanczos bandpass filter with 121 weights (e.g., Duchon 1979) was applied to the residual daily SLP and SAT time series at a given grid point. Figure S1 in the online supplemental material shows examples of application of the filter with 121 and 201 weights at a selected grid point (60°N, 91°E). It is seen that little improvement is obtained with 201 weights and using 121 weights loses fewer days of data at the beginning and end of the time series.

At a given grid point, composites for a given set of conditions (i.e., time of year, OMI amplitude, OMI phase, ENSO phase, QBO phase, and/or QDO phase) were computed by determining all qualifying days and calculating a simple average of the filtered daily SLP and SAT data. Since our main purpose is to examine how the evolution and amplitude of the MJO modulation differs for different tropospheric and stratospheric forcing conditions, composites for a given MJO phase are constructed simply by using all qualifying days when the MJO was in that phase according to the OMI. More detailed studies aimed at predicting an extratropical weather pattern following an observed developing MJO event (e.g., Cassou 2008) usually determine occurrence rates as a function of lag time from the onset of a given MJO phase. (See section 4 and Fig. S2 for an example of a lagged composite.) This is done to account more accurately for the finite propagation time of the Rossby wave train from its tropical heating source. It typically requires 2–3 weeks for the wave train to propagate to northern latitudes and fully develop (Jin and Hoskins 1995). For comparison, the mean durations of the eight MJO phases in the 38 years of NDJFMA seasons sampled here using OMI data were 4.8, 5.7, 5.4, 4.7, 4.7, 5.5, 5.3, and 4.8 days (mean: 5.1 days) and the mean duration of a complete MJO event was about 41 days. Therefore,

for example, a composited SLP or SAT response in phase 6 may actually be due to a Rossby wave train that was initiated in the tropical warm pool region in phase 3.

Statistical significance of the composites at a given grid point is assessed using a two-sided Student's t test (Student 1908). The number of degrees of freedom is not approximately equal to the number of observations because the daily observations after filtering are significantly autocorrelated. To account for this, the autocorrelation coefficient r is determined. The number of degrees of freedom, ndeg, or effective sample size of order one, is then estimated from ndeg $= N(1 - r)/(1 + r)$ (Bretherton et al. 1999, p. 2004). If the composite at a given grid point is significant at a level of 5% (95% confidence), and if the grid point is within the colored areas on the composite map, an asterisk is plotted at the grid point (see, e.g., Fig. 4 below).

As will be seen in section 4, it is useful to introduce several concise diagnostics of the MJO wave train amplitude and its modulation of extratropical SLP and SAT. This is necessary to allow an assessment of whether these characteristics for a selected set of stratospheric/tropospheric conditions differ significantly from the long-term mean or from those for an alternate set of conditions. Values of the diagnostics at a given MJO phase within a selected climate state (e.g., cool ENSO) are considered to be significantly different from the mean (calculated from all qualifying days regardless of stratospheric/tropospheric conditions) if they exceed the 95% confidence limits of the mean. The same values are considered to be significantly different from those in the opposite climate state (e.g., warm ENSO) if the values for the opposite climate state exceed the 95% confidence limits of the mean in the opposite sense (see, e.g., Figs. 6b and 6c below). Alternatively, if the values for one climate state fall outside the 95% confidence limits of the values for the opposite climate state, then they are also considered to be significantly different from those in that climate state (see, e.g., Fig. 6a below). The 95% confidence limits are estimated via a Monte Carlo procedure in which the compositing and diagnostic calculations are repeated several hundred times using randomly resampled data, as described in more detail in the sections below.

3. Normalized occurrence rates

In this section, normalized occurrence rates (i.e., the fraction of qualifying days when the MJO amplitude exceeded a chosen threshold) are calculated. The methodology is similar to that of Hood (2017, 2018), who calculated MJO occurrence rates accepting days when the OMI amplitude exceeded 1.0 standard deviations. Here, for the purpose of detecting more easily the extratropical

consequences of the MJO during NDJFMA, a minimum OMI amplitude threshold of 1.5 is adopted (see section 4 for further explanation).

Results are shown in Fig. 1 for cool (warm) ENSO phases, easterly (westerly) QBO phases, and minimum (maximum) QDO phases as defined in section 2. Error bars are two standard deviation limits representing approximate 95% confidence bounds, estimated using a Monte Carlo procedure as described by Hood (2017). The total number of qualifying days (regardless of MJO amplitude) when ENSO, the QBO, and the QDO were in a given state are listed in the figure for each calculated occurrence rate.

In the top panel of Fig. 1, occurrence rates are shown for the two phases of each forcing. In the case of ENSO, occurrence rates of events with OMI > 1.5 are nearly the same in the two phases. This agrees with an analysis by Son et al. (2017), who found that, although ENSO mainly controls the interannual variation of tropical convection, the overall level of MJO activity in the Indo-Pacific region is not very sensitive to the phase of ENSO. However, as shown by the same authors (see also Yoo and Son 2016), the QBO exerts a stronger influence on mean MJO activity with larger occurrence rates and reduced static stability in the tropical lower stratosphere during the easterly QBO phase ($u50 < 0$). As seen in the figure, the QBOE ($u50 < 0$) occurrence rate for OMI > 1.5 is nearly 45% while that for QBOW ($u50 > 0$) is about 30%. The error bars overlap only slightly so the difference is almost significant at 95% confidence. Possible reasons why larger occurrence rates are obtained during QBOE than during QBOW are discussed in section 6.

In the case of the QDO, a larger mean occurrence rate is obtained for SMIN conditions (defined in section 2 as $F205 < 10.1 \, \text{mW m}^{-2} \text{nm}^{-1}$) than for SMAX conditions (defined as $F205 > 10.5 \, \text{mW m}^{-2} \text{nm}^{-1}$). However, the difference is only significant at the ~1 standard deviation level (~68% confidence). Repetitions of the calculation excluding the two SMAX years following El Chichón and Pinatubo produce very similar results. Possible reasons why the SMIN phase should produce more strong MJO events are discussed by Hood (2018) and summarized in section 7.

In the bottom panel of Fig. 1, occurrence rates are shown for different combinations of the three forcings. These combinations are selected according to the results in the top panel to maximize or minimize the net total forcing. Error bars are somewhat larger than those in the top panel because of the reduced number of qualifying days when more than one forcing is considered. For the ENSO/QDO combinations (first comparison in the bottom panel), the occurrence rates for SMIN/cool
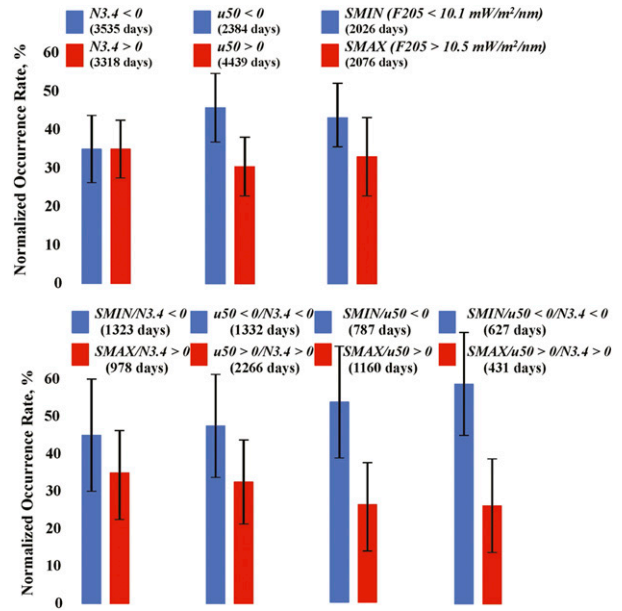

FIG. 1. Normalized occurrence rates (i.e., fraction of qualifying days in 1979–2016) in percent for daily MJO events with OMI amplitudes >1.5 during the NDJFMA extended boreal winter season when the stated conditions existed. The number of qualifying days with any OMI amplitude in each category is given.

ENSO and SMAX/warm ENSO are not very different from those obtained for SMIN and SMAX alone. Similarly, except for larger error bars, the QBOE/cool ENSO and QBOW/warm ENSO comparison is not very different from the QBOE and QBOW comparison in the top panel. However, the QBO/QDO combination (third plot of the bottom panel) yields a noticeable increase in the difference between SMIN/QBOE and SMAX/QBOW relative to that obtained for either QBOE versus QBOW or SMIN versus SMAX. A slightly larger difference is obtained for SMIN/QBOE/cool ENSO relative to SMAX/QBOW/warm ENSO, although the numbers of qualifying days in these categories are relatively low and the error bars are large.

4. Mean MJO phase composites

Figure 2 plots the individual MJO phase composites of 20–100-day filtered SLP and SAT anomalies at northern latitudes for all NDJFMA days in 1979–2016 when the OMI amplitude exceeded 1.5 (2361 days). 2361 days represents about 34.3% of days in NDJFMA for these 38 years. For comparison, when OMI amplitudes >1.0 are allowed, 4060 days are qualified, which is about 59% of all days. The number of degrees of freedom in each phase group in Fig. 2 is sufficiently large that virtually all of the colored areas are significant at more than 95% confidence according to a two-sided t test. For this

(a) Sea Level Pressure
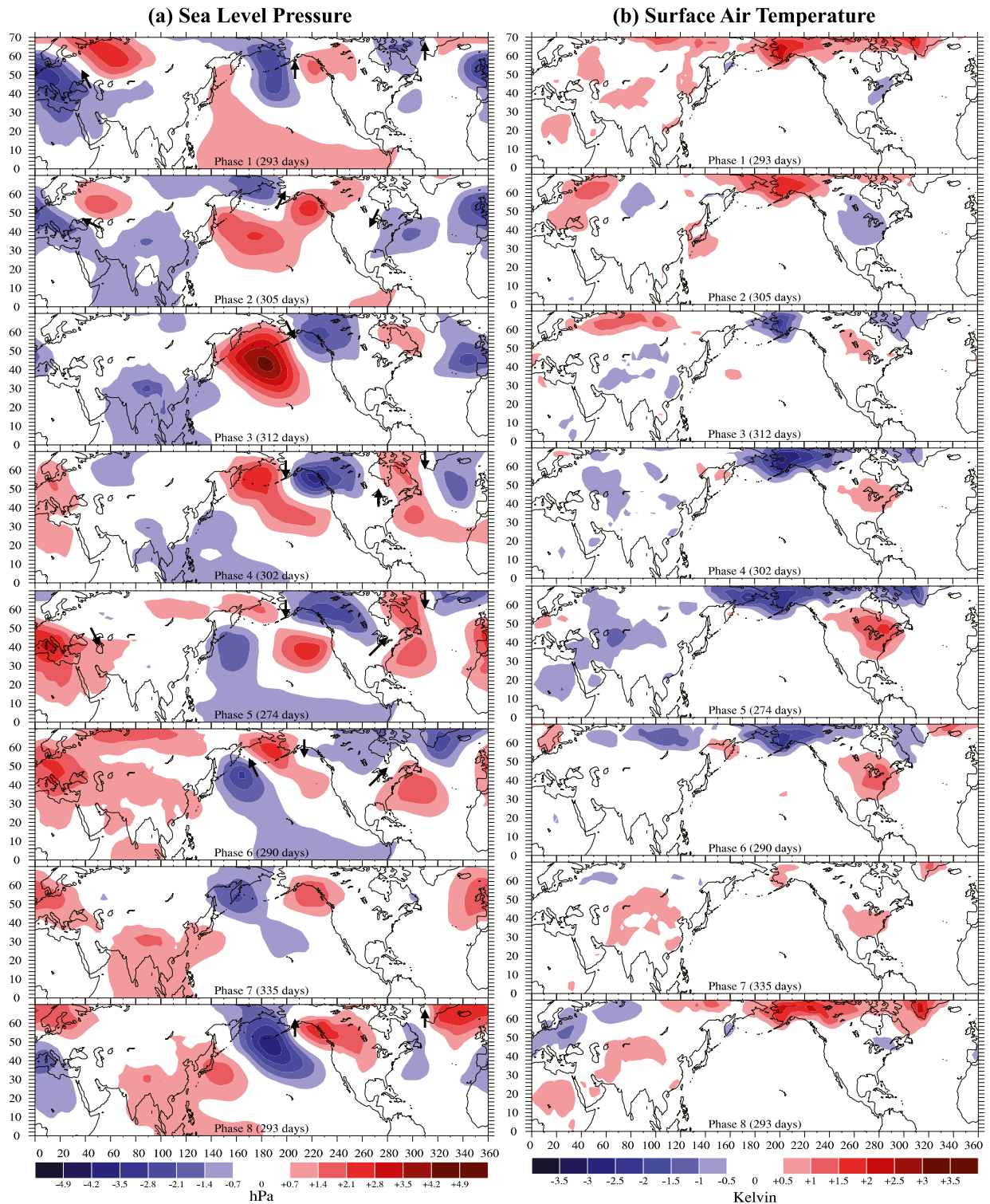
(b) Surface Air Temperature

FIG. 2. Composites of the 20–100-day filtered November–April 1979–2016 (a) sea level pressure and (b) 2-m surface air temperature anomalies for the eight phases of the MJO when the OMI amplitude was >1.5. Arrows indicate the approximate direction of near-surface anomalous geostrophic flow. The number of days used to construct the composites is indicated in each panel.

reason, no significance asterisks are shown in this figure. In Fig. 2a, arrows are superposed between selected SLP anomalies indicating the approximate direction of near-surface anomalous geostrophic flow.

As mentioned in section 2, these composites are constructed at zero phase lag. To illustrate how the composites would change if a finite lag is considered, Fig. S2 shows the equivalent of Fig. 2 when the composited SLP and SAT anomalies are lagged by 10 days relative to the date of a given MJO phase. It is seen that the overall evolution of the SLP and SAT anomalies is similar to that in Fig. 2 but is shifted earlier in time by one or two MJO phases.

Considering first the SLP composites in Fig. 2a, a positive (anticyclonic) anomaly develops with maximum amplitude at phase 3 in the North Pacific near the location of the climatological Aleutian low (e.g., Moon et al. 2011). It gradually declines in intensity thereafter and is replaced by a negative (cyclonic) anomaly with maximum amplitude in phase 8. By phase 2, a negative SLP anomaly develops over southern Eurasia, extending into the tropical Indian Ocean, and shifts eastward with increasing MJO phase, reaching the central to eastern Pacific by phase 6. This tropical low pressure area corresponds to the zone of maximum MJO convective activity. It is largest in area in phases 2 and 3; the associated Rossby wave train is most well defined in phase 3. It consists of a series of alternately negative and positive anomalies with wavelength ~10 000 km extending northeastward across the Pacific from the MJO convective center and then eastward across North America and the Atlantic. In phase 4, a positive NAO pattern develops (positive SLP anomaly over Portugal, negative anomaly over Iceland), consistent with the analyses of Cassou (2008) and Lin et al. (2009). The positive anomaly over southern Europe and North Africa covers the entire Mediterranean and Black Sea areas, expanding eastward in phases 5 and 6. It shifts southeastward to the Maritime Continent region by phases 6 and 7. The NAO pattern is mainly negative in phases 8, 1, and 2 and is clearly positive in phases 4, 5, and 6.

A simple diagnostic of the overall strength of the wave train is the root-mean-square (RMS) amplitude of the filtered and composited anomaly pattern over the whole region considered here (0°–70°N, all longitudes). Figure 3a plots this amplitude as a function of MJO phase for the SLP anomalies of Fig. 2a at all grid points where anomalies exceed 0.5 hPa in absolute magnitude. The largest amplitude occurs in phase 3 when the North Pacific anticyclonic anomaly peaks in intensity. As would be expected, the strength of the wave train depends on MJO amplitude (Fig. 3b) and is largest for OMI > 2.

However, the wave train amplitude diagnostic in Fig. 3a is not ideal for characterizing the modulation of intraseasonal climate by the MJO. For the latter purpose, we consider an alternate diagnostic consisting of the mean intraseasonal SLP anomaly over a given region. As shown in Fig. 3c, the value of this diagnostic over the whole analyzed region yields a weak but smooth modulation characterized by negative values for low MJO phases and positive values for later MJO phases. (The average over all MJO phases is approximately zero since the filtered time series with seasonal cycle minimized has a zero mean.) Averages of SLP anomalies over the North Pacific (not shown in Fig. 3c) are strongly modulated with positive values in MJO phase 3 and negative values in phase 8. This average could be adopted as a useful diagnostic of the MJO modulation of intraseasonal climate in that region. However, as shown in the figure, another large modulation is found for averages over the North Atlantic/Eurasian sector. An especially large modulation is obtained for averages over a region extending from approximately 30° to 70°N, 80°W to 80°E. This specific average is therefore adopted as a diagnostic of the MJO modulation of regional intraseasonal climate in the remainder of the paper.

Considering next the SAT composites in Fig. 2b, a series of positive and negative temperature anomalies evolve with MJO phase. These anomalies have been documented and interpreted in previous studies. Over eastern North America, a cooling anomaly is present in phases 1 and 2, evolving into a warm anomaly that persists through phase 7 with maximum amplitude in phase 5 (Zhou et al. 2012). At high latitudes from Alaska to Greenland, a warm anomaly is present in phases 1 and 2, evolving into a strong cooling anomaly in phases 4 to 6 before returning to a warm anomaly in phase 8 (e.g., Vecchi and Bond 2004). A warming anomaly is present over east Asia in phases 1, 2, and 8 while a strong cooling anomaly develops over eastern Europe in phases 3–5 (Seo et al. 2016).

As shown quantitatively by Yoo et al. (2012) and Seo et al. (2016), the SAT anomalies in Fig. 2b are caused by dynamical processes associated with the propagating Rossby wave trains. In particular, as can be seen by comparing these anomalies to the approximate geostrophic flow directions (arrows) in Fig. 2a, horizontal temperature advection plays a major role. During phases 1 and 2 when SLP anomalies yielding a negative NAO pattern prevail, cyclonic flow due to intensified low pressure in the North Atlantic favors southward advection of cooler air across eastern North America. During phases 3–6 when a positive NAO pattern dominates, the low pressure anomaly is replaced with a high pressure anomaly, which, in combination with a cyclonic low pressure anomaly over northwestern Canada, results
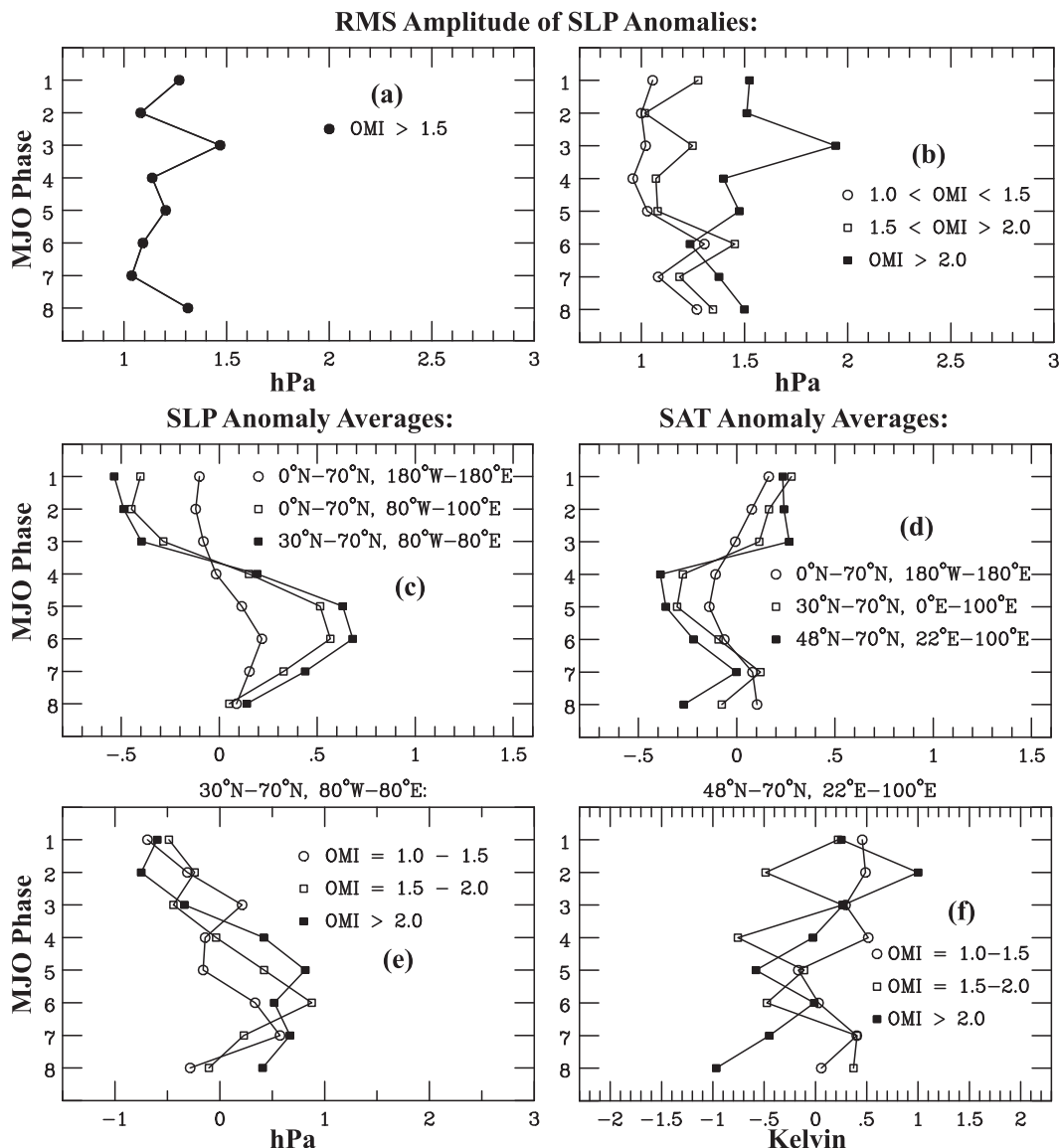
RMS Amplitude of SLP Anomalies:

SLP Anomaly Averages: **SAT Anomaly Averages:**

FIG. 3. (a) RMS amplitude of the SLP anomaly composites of Fig. 2a at all grid points where anomalies exceed ±0.5 hPa. (b) As in (a), but for different ranges of the MJO amplitude. (c) Averages of the SLP anomaly composites of Fig. 2a over selected geographic regions. (d) As in (c), but for the SAT composites of Fig. 2b. (e) Dependence of the most strongly modulated SLP anomaly average identified in (c) on MJO amplitude. (f) Dependence of the most strongly modulated SAT anomaly average identified in (d) on MJO amplitude.

in northward advection of warmer air across the same area. The latter cyclonic anomaly, together with the anticyclonic anomaly over the North Pacific, produces a southeastward cooling flow across Alaska. A similar southeastward cooling flow occurs over the Labrador Sea and southern Greenland. The high and low pressure anomalies that define the positive NAO pattern produce a northeastward warming flow over northern Europe. These anomalous flows continue until the NAO pattern becomes neutral again in phase 7.

As the tropical low pressure anomaly representing the MJO convective center moves into the central Pacific in phase 5, the Rossby wave train is compressed into a smaller area. The North Atlantic anticyclonic anomaly and the northwestern Canada cyclonic anomaly are strengthened, resulting in a stronger warming anomaly over eastern North America. Meanwhile, the North Atlantic anticyclonic anomaly extends over the Mediterranean and Black Sea region producing anticyclonic flow southwestward across western Eurasia, leading to a

cooling anomaly in the same region with maximum amplitude also in phase 5. As the convective center moves farther into the eastern Pacific in phase 6, the wave train weakens and the warming (cooling) anomaly over eastern North America (western Eurasia) also weakens. By phase 8, the tropical positive pressure anomaly and associated weakened convection over the Maritime Continent excite a Rossby wave train with opposite sign to that in phases 3 and 4, producing a cyclonic anomaly in the North Pacific and a negative NAO pattern. Warming anomalies are now present in the Arctic, extending from Alaska to Greenland, replacing the cooling anomalies present during phases 3–6.

The MJO modulation of SAT anomalies in Fig. 2b can be characterized in various ways depending on the region of interest (e.g., using the mean SAT anomaly over Alaska for the North Pacific region). Figure 3d plots the mean SAT anomaly over a series of regions including the entire mapped region and several regions in Eurasia. An especially large modulation is obtained for averages over the northern Eurasian region extending over 48°–70°N, 22°–100°E. It is closely related to the northern Eurasian SLP anomaly diagnostic of Fig. 3c because, as will be seen in the following sections, it depends sensitively on the strength of the anticyclonic SLP anomaly over Eurasia. This average is therefore used as a second diagnostic of the MJO modulation of regional intraseasonal climate in the remainder of the paper.

As shown in Figs. 3e and 3f, the MJO modulation of the chosen SLP and SAT diagnostics is stronger for OMI amplitudes exceeding about 1.5. This is the primary justification for adopting a threshold of OMI = 1.5 standard deviations for the SLP and SAT anomaly composites. On the other hand, as also shown in Figs. 3e and 3f, the MJO modulation of either diagnostic does not increase much when the allowed OMI range is increased from 1.5–2.0 to > 2.0.

5. Separation by ENSO phase

Previous work has shown that El Niño–Southern Oscillation (ENSO) both influences and is influenced by the MJO. ENSO influences the longitudinal distribution of tropical MJO activity such that it extends farther eastward during El Niño winters but contracts westward and northward during La Niña winters (Son et al. 2017, and references therein). On the other hand, enhanced MJO activity in spring favors an eastward-expanded warm pool and surface westerly wind anomalies that assist in initiating El Niño in the subsequent fall and winter seasons (Hendon et al. 2007; Pohl and Matthews 2007). The extratropical circulation anomalies that develop during the evolution of a given MJO event are significantly

dependent on the phase of ENSO as shown by both model simulations and observational analyses (e.g., Tam and Lau 2005; Roundy et al. 2010; Moon et al. 2011). Overall, the excitation of the Rossby wave train is enhanced under La Niña conditions during early MJO phases when MJO convection in the Indian Ocean is stronger and extends more northward. Storm track activity is also more intense in the western (eastern) North Pacific under La Niña (El Niño) conditions during the early phases of the MJO (Takahashi and Shirooka 2014). Statistical evidence has been reported for a dependence on ENSO phase of the MJO influence on atmospheric river events (Baggett et al. 2017), winter blocking events (Henderson and Maloney 2018), and North Atlantic/European weather regimes (Lee et al. 2018).

Figures 4 and 5 are SLP and SAT composites similar to those of Fig. 2 but considering only days when ENSO was either in its cool phase (defined here as N3.4 < 0) (Figs. 4a and 5a) or its warm phase (N3.4 > 0) (Figs. 4b and 5b). The plotted asterisks indicate those grid points that are statistically significant at 95% confidence according to the Student's t-test methodology described in section 2. The number of qualifying days in each MJO phase is reduced by a factor of about 2 but almost all colored areas remain statistically significant in both figures. For example, for the warm ENSO SLP composite in phase 3 (Fig. 4b, third panel), the North Pacific maximum is about 3.3 hPa at 48°N, 184°E with a standard deviation of 4.9 hPa. The number of qualifying days is 140 and the autocorrelation coefficient of the time series at this location is about 0.8 so the number of degrees of freedom is approximately 15. The minimum t value required for 95% confidence is about 2.13 and the actual t value is larger than this.

A visual comparison of Figs. 4a and 4b indicates that the MJO-induced Rossby wave train is enhanced under cool ENSO conditions relative to that under warm ENSO conditions. This impression is supported by the RMS amplitude calculations of Fig. 6a, which show that the amplitude in all MJO phases is larger under cool ENSO conditions than under warm ENSO conditions. In most phases, the cool ENSO amplitude falls outside of the 95% confidence bounds of the warm ENSO amplitudes. The latter are estimated via a Monte Carlo procedure in which calculations are repeated several hundred times retaining the observed MJO OMI amplitudes and phases but randomizing the N3.4 daily values. The number of qualifying days is generally larger for cool ENSO conditions than for warm ENSO conditions. This also supports the reality of the enhancement under cool ENSO conditions since a smaller number of qualifying days can bias a composite toward larger relative anomaly amplitudes (e.g., Roundy et al. 2010).
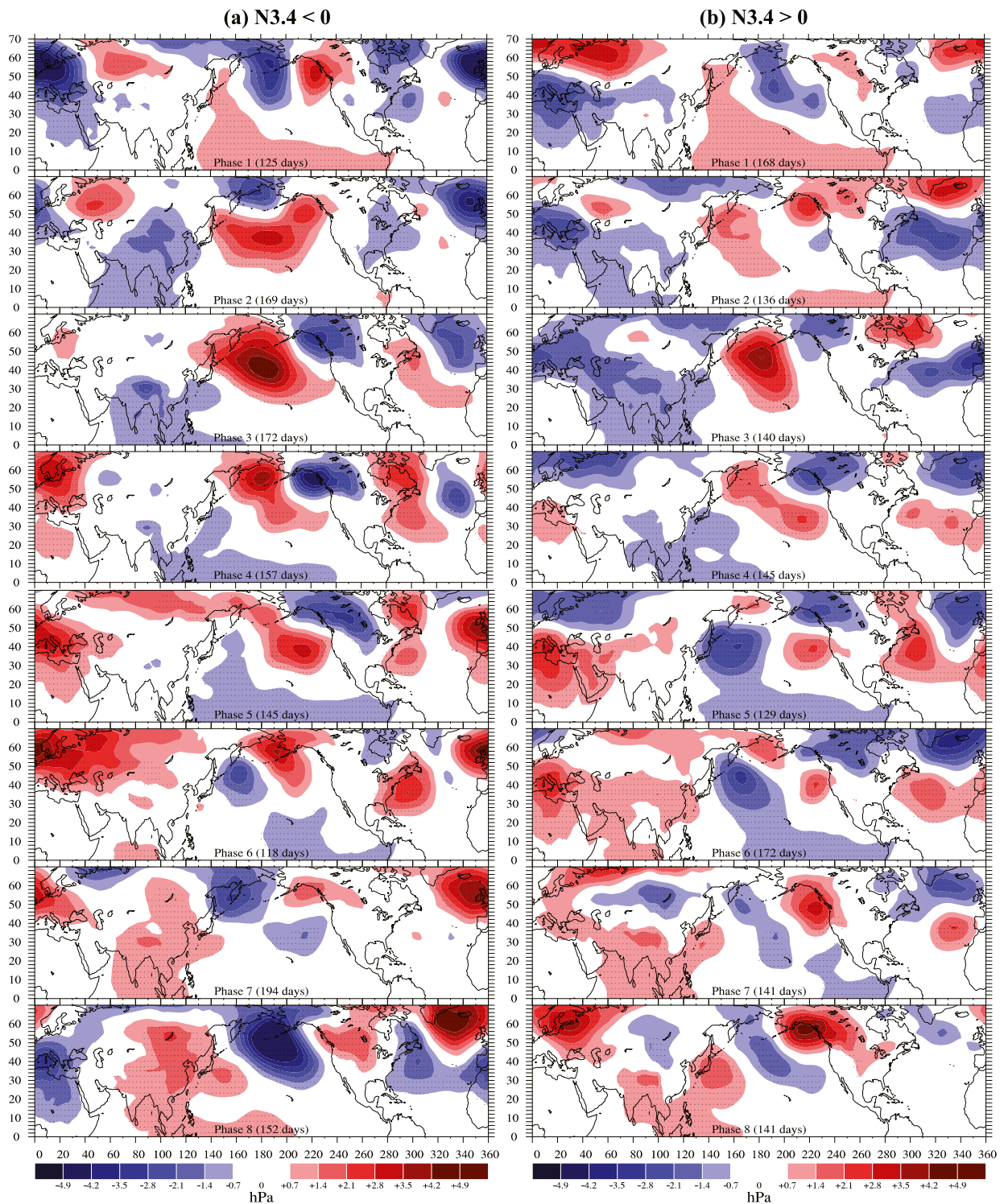
(a) N3.4 < 0 (b) N3.4 > 0

FIG. 4. Sea level pressure anomalies as in Fig. 2a but separated according to the phases of ENSO: (a) cool ENSO (N3.4 < 0) and (b) warm ENSO (N3.4 > 0). Asterisks indicate grid points where the composited means are significant at more than 95% confidence according to a two-tailed Student's t test (section 2).
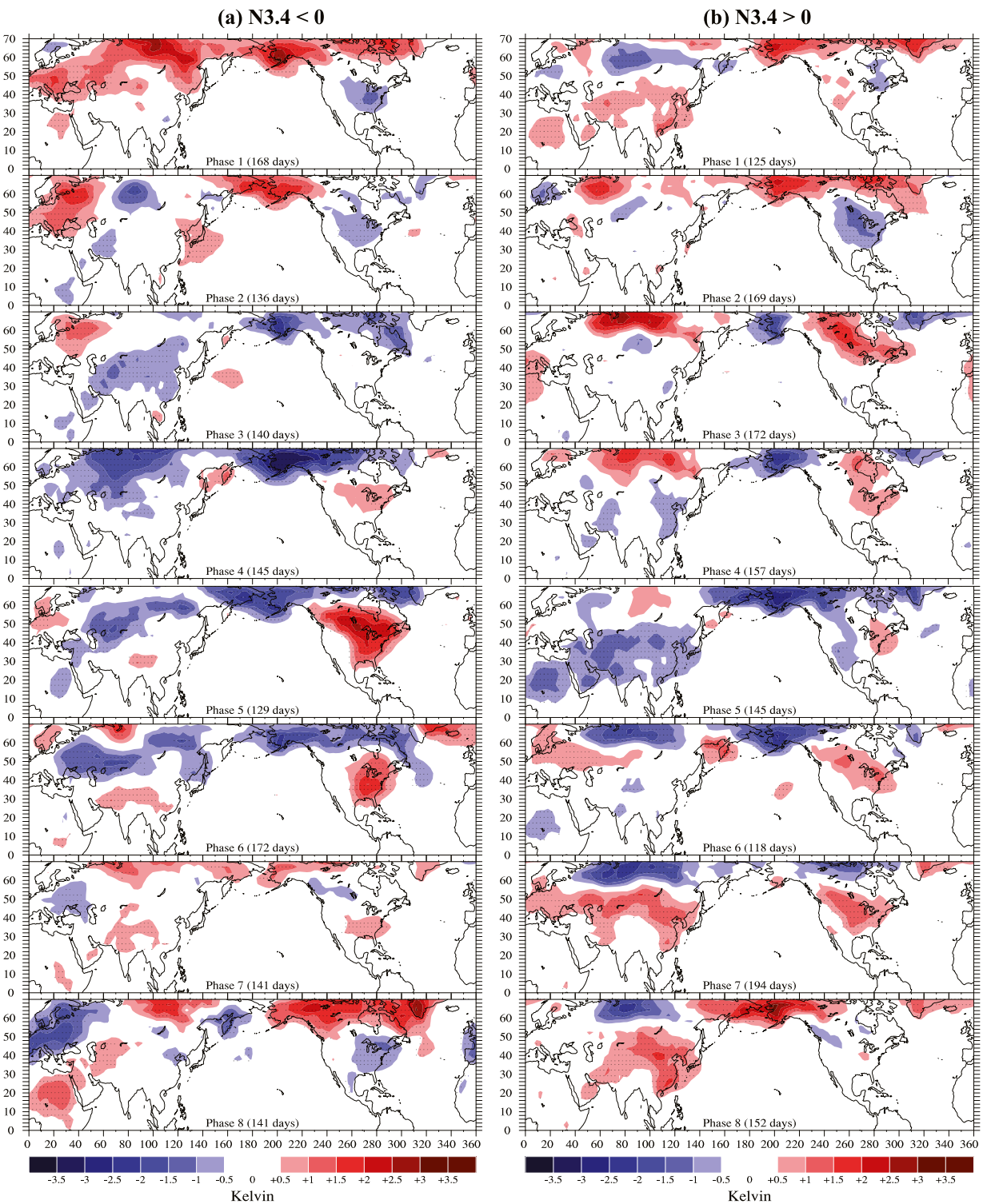
(a) N3.4 < 0　　　　　　　　　　　　　　　　**(b) N3.4 > 0**

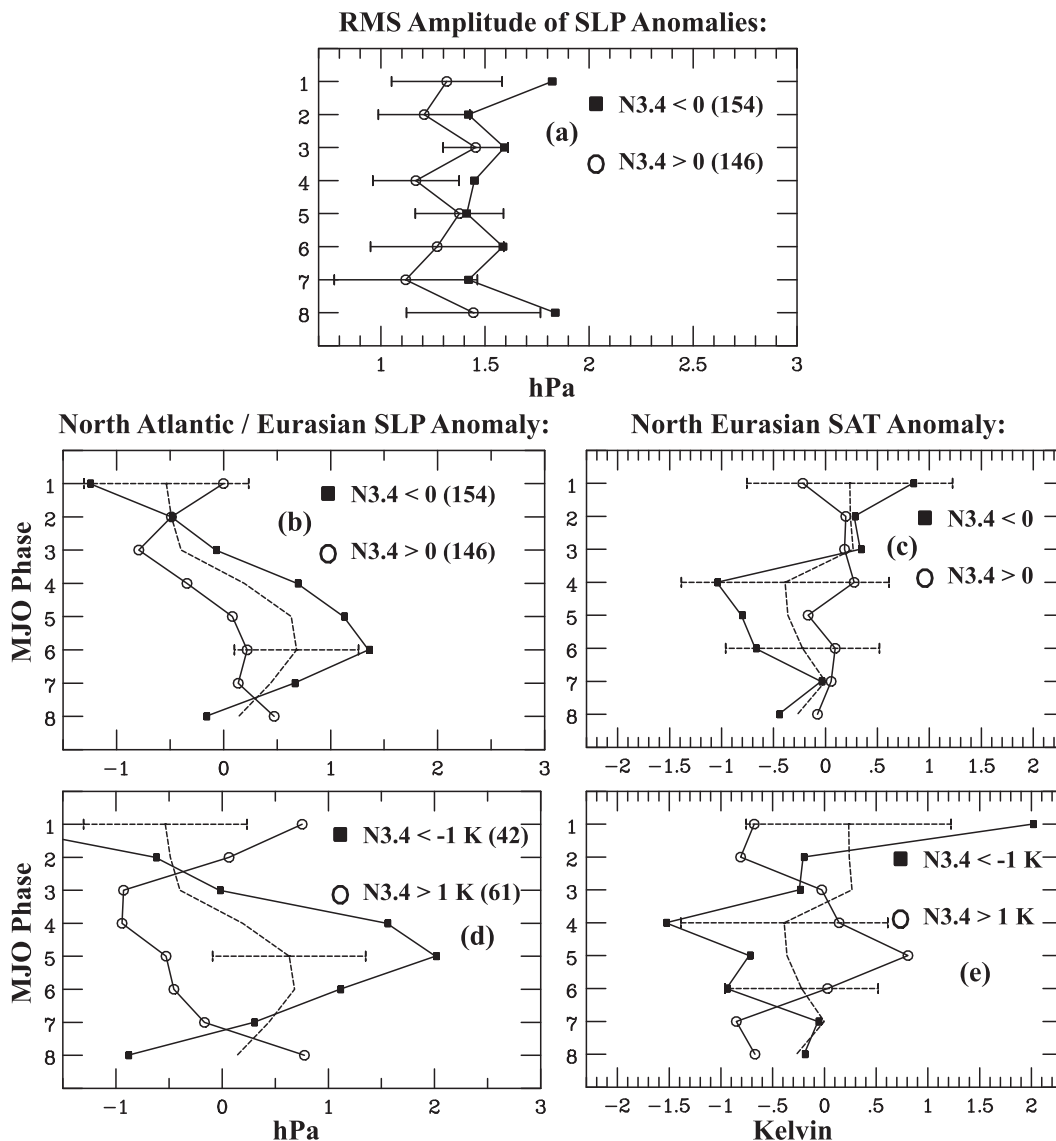FIG. 5. As in Fig. 4, but for surface air temperature anomalies.

FIG. 6. SLP and SAT diagnostics separated by ENSO phase. (a) RMS amplitude of the SLP anomaly composites of Figs. 4a and 4b; numbers in parentheses are the mean numbers of qualifying days in each of the eight MJO phases. (b) North Atlantic/Eurasian mean sea level pressure anomaly (defined in Fig. 3) separated by ENSO phase for days when the MJO amplitude exceeded 1.5; the dashed line is the mean anomaly amplitude when all days are considered. (c) As in (b), but for the northern Eurasian 2-m surface air temperature anomaly diagnostic (defined in Fig. 3). (d),(e) As in (b),(c), but for more active ENSO conditions.

As demonstrated originally by Moon et al. (2011), under La Niña conditions, the North Pacific anticyclonic anomaly that typically forms in MJO phase 3 becomes "gigantic" with consequent effects on surface air temperature and precipitation along the coasts of both North America and east Asia. Although the composites of Fig. 4a for N3.4 < 0 only represent cool ENSO conditions rather than true La Niña conditions, the North Pacific anticyclonic anomaly in the third panel is indeed enhanced and enlarged relative to the mean anomaly

shown in the third panel of Fig. 2a. Under warm ENSO (N3.4 > 0) conditions, the anticyclonic anomaly is much smaller (Fig. 4b, third panel) and has little effect on North Pacific coastal regions. Conversely, as also seen in Fig. 4a, by MJO phase 7, a strong cyclonic anomaly forms over the North Pacific for N3.4 < 0, producing cooling and increased precipitation over Japan.

In Fig. 4a during MJO phases 4–6, a strong positive SLP anomaly develops over northern Eurasia, consistent with farther eastward propagation of the wave train

and a stronger NAO response under cool ENSO conditions. A strong negative SLP anomaly develops in the same area in phases 1–2. In Fig. 5a, over Eurasia, a stronger cooling anomaly is present during MJO phases 4–6 and a stronger warming anomaly is found in phases 1–2 than is the case in Fig. 5b. The stronger Eurasian SLP anomalies and farther eastward propagation are not caused solely by larger-than-average MJO amplitudes under cool ENSO conditions because, for the considered NDJFMA season and minimum OMI amplitude of 1.5, the mean OMI amplitude under cool ENSO conditions (2.09) was nearly the same as that under warm ENSO conditions (2.08). This near equality is to be expected from the occurrence rate calculation results of section 3 (Fig. 1a).

In Figs. 6b and 6c, both the North Atlantic/Eurasian SLP diagnostic and the northern Eurasian SAT diagnostic identified in Fig. 3 are plotted as a function of MJO phase for the two ENSO phases. In Fig. 6b, the MJO modulation of the SLP anomaly diagnostic is stronger for the cool ENSO case than for the warm ENSO case. This is consistent with a stronger Rossby wave amplitude near the end of its propagation path under cool ENSO conditions. For comparison, the mean SLP diagnostic is also shown as a dashed line. The 95% confidence limits on the means shown in the figure are estimated via a Monte Carlo procedure in which the observed MJO OMI amplitudes and phases are replaced with randomly selected values. Both the cool ENSO and warm ENSO SLP diagnostics approach significance at 95% confidence on opposite sides of the mean for MJO phases 1 and 6. In Fig. 6c, the MJO modulation of the SAT anomaly diagnostic is also stronger for the cool ENSO case as would be expected since the SLP and SAT diagnostics are closely related. As shown in Figs. 6d and 6e, these differences become more significant when "cold" (N3.4 < −1 K) and "very warm" (N3.4 > 1 K) ENSO conditions are considered, confirming the reality of the ENSO influence on the MJO-induced wave train and its effect on intraseasonal climate in the North Atlantic/Eurasian sector.

The results of Figs. 4–6 are largely consistent with several recent studies when differences in analytic techniques are considered. A study of the MJO impact on high-latitude winter blocking during ENSO events (Henderson and Maloney 2018) showed that the Rossby wave source in the subtropical upper tropospheric jet region is stronger during La Niña than during El Niño, which they attributed to stronger tropical convection and a stronger and sharper jet during La Niña. This resulted in a stronger teleconnection pattern in 30–70-day bandpass filtered 500-hPa geopotential height fields during La Niña [see the top panels of their Figs. 6–9 in

Henderson and Maloney (2018)]. A recent study by Lee et al. (2018) has extended the original analysis of Cassou (2008) to consider the ENSO influence on the MJO teleconnection to weather regimes in the North Atlantic and Europe. They find that the MJO teleconnections to the positive and negative NAO states are mainly found during neutral and warm ENSO conditions. This appears to differ from our results, which show strongly positive NAO phase tendencies in MJO phases 4 and 5 under cool ENSO conditions (Fig. 4a, panels 4 and 5). However, our analysis uses 20–100-day filtered SLP data whereas their study used unfiltered geopotential height data at 500 hPa. They also only evaluated the sign of the NAO rather than considering its amplitude.

6. Separation by QBO phase

The stratospheric quasi-biennial oscillation (QBO) consists of alternating easterly (QBOE) and westerly (QBOW) equatorial zonal wind regimes at heights ranging from about 16 to 50 km with a period averaging about 28 months. It is the dominant mode of interannual variability of the equatorial stratosphere (Baldwin et al. 2001). Because the QBO winds are in thermal wind balance, an induced meridional circulation exists with equatorial ascent and adiabatically reduced temperatures during QBOE while descent and higher temperatures occur during QBOW (Plumb and Bell 1982). The adiabatic change of temperature results in reduced static stability in the tropical uppermost troposphere and lower stratosphere (UTLS) during QBOE and increased static stability in QBOW (e.g., Gray et al. 2018). The phase of the QBO at a given time depends strongly on altitude. As explained by Baldwin et al. a single monitoring level of 40 or 50 hPa is usually chosen to yield a relatively strong signal in the extratropical northern stratosphere.

Recent work has shown that the mean boreal winter (December–February) MJO propagates eastward more slowly and has a larger amplitude and/or occurrence rate during QBOE than during QBOW (Liu et al. 2014; Yoo and Son 2016; Nishimoto and Yoden 2017; Hood 2017; Zhang and Zhang 2018). This observed modulation of the MJO by the QBO is qualitatively consistent with that found previously for the QBO influence on tropical convection in general (Giorgetta et al. 1999; Collimore et al. 2003; Liess and Geller 2012; Nie and Sobel 2015). Evidence for an influence of the QBO on the MJO modulation of atmospheric river events (Baggett et al. 2017) and North Pacific storm track activity (Wang et al. 2018a,b) has been reported. The latter authors find that the mean position of the storm track during a given winter shifts poleward during QBOE relative to that during QBOW. Also, the MJO modulation of the storm

track activity, which consists of a northward shift during the early phases of the MJO followed by a southward shift during the later phases (e.g., Guo et al. 2017), has a larger amplitude during QBOE than during QBOW.

Possible mechanisms for the QBO influence on MJO convection include reduced static stability in the UTLS and weaker vertical wind shear across the tropopause during QBOE (Yoo and Son 2016; Nishimoto and Yoden 2017). In addition, QBOE-induced temperature decreases near the tropopause may indirectly modify the thermodynamic efficiency and hence the potential intensity of deep convective systems, consistent with the suggested effect of long-term tropopause cooling on tropical cyclone activity (Emanuel et al. 2013). MJO convection can extend vertically to higher altitudes than typical tropical convection, effectively increasing the tropopause height (e.g., Madden and Julian 1972, their Fig. 16), thereby possibly contributing to its increased susceptibility to stratospheric influences. Positive feedbacks involving cloud-radiative effects (e.g., Giorgetta et al. 1999) and/or MJO influences on the strength of the residual meridional (Brewer–Dobson) circulation and its associated tropical upwelling rate (e.g., Hood 2018) may serve to amplify the QBO–MJO connection.

Figures 7 and 8 show results analogous to the ENSO results in Figs. 4 and 5 for QBOE (u50 < 0) and QBOW (u50 > 0) conditions, respectively. Since the QBO spends more time in QBOW than in QBOE, the number of qualifying days during most MJO phases is somewhat larger for Figs. 7b and 8b than for Figs. 7a and 8a. However, the number is still large enough during QBOE that, even after accounting for autocorrelation, the composites are significant at 95% confidence at most grid points within the colored areas (see the plotted asterisks). For example, for the QBOW SLP composite in phase 3 (Fig. 7b, third panel), the North Pacific maximum is about 3.1 hPa at 42°N, 184°E with a standard deviation of 4.4 hPa. The number of qualifying days is 178 and the autocorrelation coefficient of the time series at this location is about 0.76 so the number of degrees of freedom (section 2) is approximately 24. The minimum t value required for 95% confidence is about 2.06 and the actual t value is larger than this.

Comparing Figs. 7a and 7b, during phases 3–8, the positive SLP anomalies are generally larger in amplitude, more numerous, and extend farther to the east into the North Atlantic/Eurasian sector during QBOE than during QBOW. This is similar in several respects to those obtained for cool ENSO conditions in Fig. 4a. For example, the North Pacific anticyclonic anomaly is again larger in area in phase 3 in Fig. 7a than it is in Fig. 7b. The North Atlantic low pressure anomaly is again stronger in phases 1 and 2 in Fig. 7a than in Fig. 7b. A strong positive

anticyclonic SLP anomaly develops in phase 6 over northern Eurasia at 60°N in Fig. 7a as was the case under cool ENSO conditions in Fig. 4a. This anomaly is absent in both Figs. 4b and 7b, consistent with weaker eastward propagation of the wave train during warm ENSO and westerly QBO conditions.

As shown in Fig. 9a, the RMS amplitude diagnostic indicates an overall stronger wave train under QBOE conditions relative to QBOW conditions during MJO phases 1–6. The amplitudes during QBOE fall near or outside the 95% confidence error limits of the QBOW amplitudes (estimated in a manner analogous to the warm ENSO error limits of Fig. 6a) during phases 1, 2, 5, and 6.

Comparing the corresponding SAT anomalies in Fig. 8a (QBOE) with those in Fig. 8b (QBOW), the QBOE anomalies in phases 4 to 6 are again stronger than the corresponding QBOW anomalies, especially over northern Eurasia, as was found for cool ENSO conditions in Fig. 5a. Both the QBOE and QBOW SAT anomalies evolve in a manner similar to those of the corresponding cool and warm ENSO anomalies of Fig. 5. As was the case for the cool ENSO composites of Figs. 4a and 5a, the stronger SLP and SAT anomalies found for QBOE are not attributable solely to larger MJO amplitudes because the mean OMI amplitude for OMI > 1.5 under QBOE conditions (2.15) was only about 5.9% larger than that under QBOW conditions (2.03).

Figures 9c and 9d show regional SLP and SAT diagnostic results for the two QBO phases analogous to the ENSO results of Figs. 6b and 6c. As was the case for the cool ENSO results, the MJO modulation of both diagnostics is much stronger for the easterly QBO phase. In phases 5 and 6, the QBOE SLP diagnostic value lies near the 95% confidence error limit on the positive side of the mean while the QBOW SLP diagnostic lies near the error limit on the negative side. As shown in Figs. 9e and 9f, this difference increases when only active QBO conditions (u50 < −10 m s^{-1} or u50 > 5 m s^{-1}) are considered, supporting the reality of the QBO influence. Finally, Figs. 9b, 9g, and 9h repeat the calculations of Figs. 9a, 9c, and 9d for combined u50 < 0/N3.4 < 0 and u50 > 0/N3.4 > 0 conditions. For all three diagnostics, the difference in the MJO modulation is enhanced when the two forcings are working together, especially in phases 5 and 6. Figures S3 and S4 show the actual SLP and SAT MJO phase composites for combined QBOE/cool ENSO and QBOW/warm ENSO conditions in a format similar to those of Figs. 4 and 5 for ENSO alone and Figs. 7 and 8 for the QBO alone. The enhancement of the MJO modulation for combined QBO/ENSO conditions is visually evident in these figures.
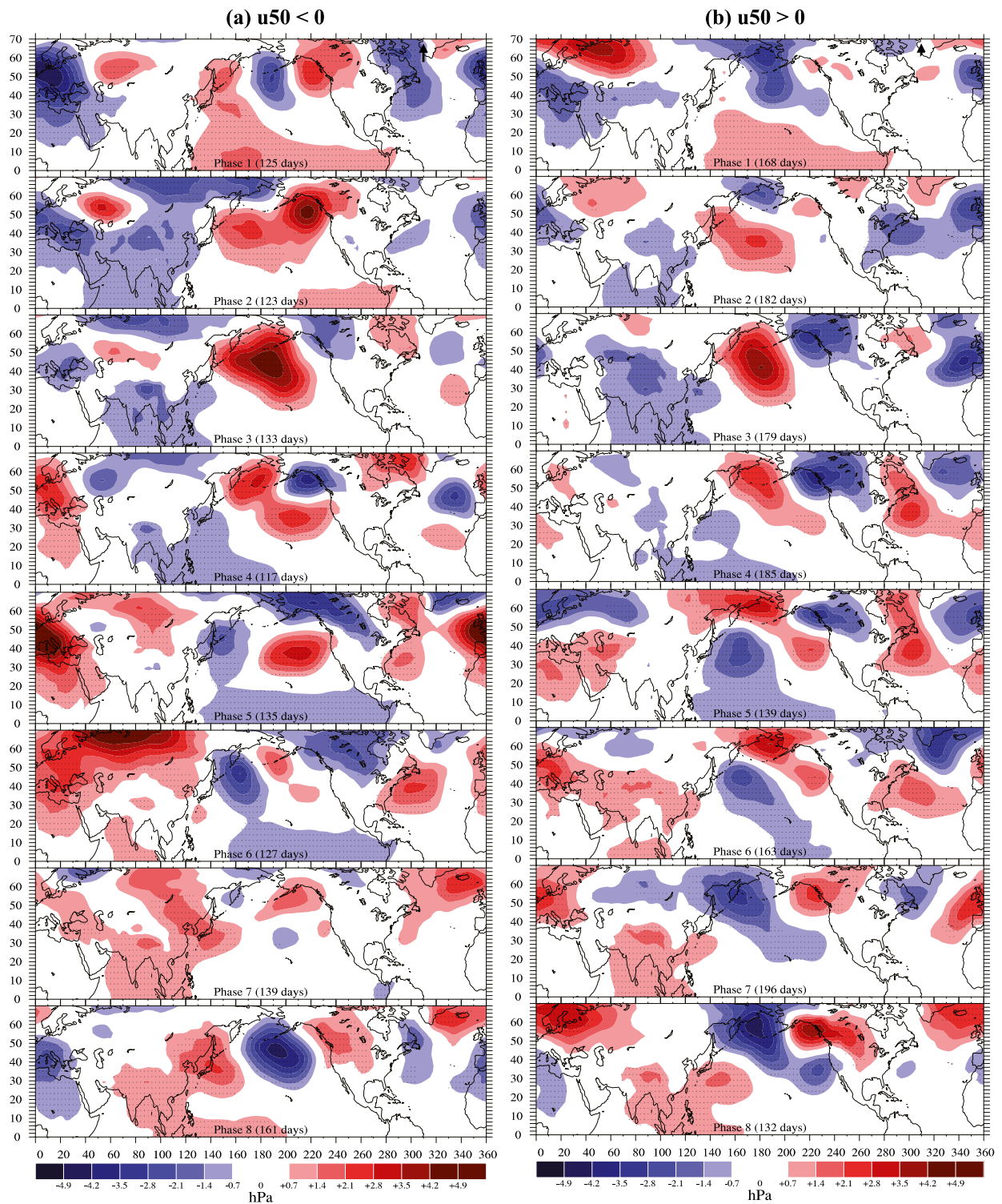
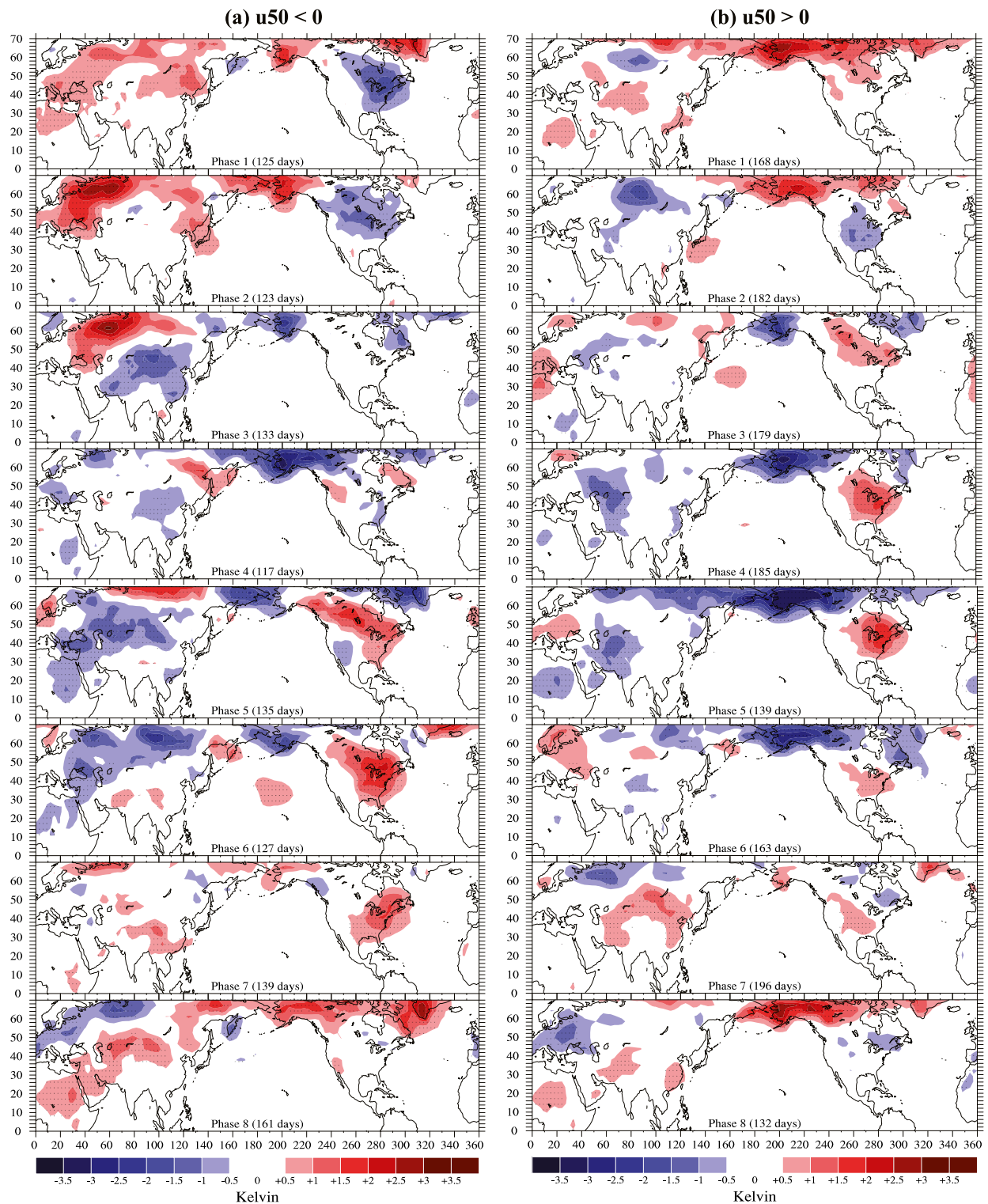FIG. 7. Sea level pressure anomalies as in Figs. 2a and 4 but separated according to the phase of the QBO: (a) easterly phase (u50 < 0) and (b) westerly phase (u50 > 0).

(a) u50 < 0 **(b) u50 > 0**

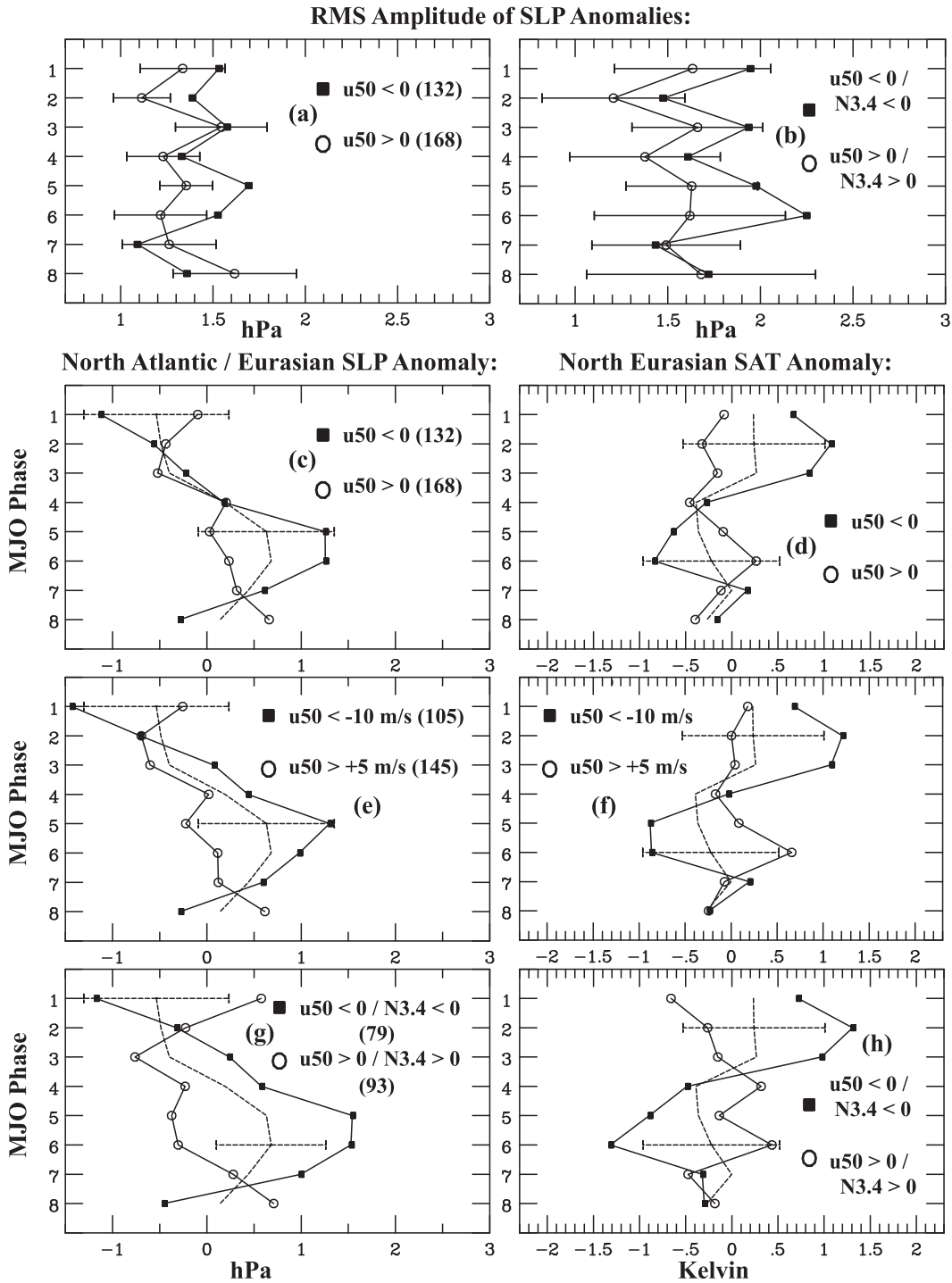FIG. 8. Surface air temperature anomalies as in Figs. 2b and 5 but separated according to the phase of the QBO: (a) easterly phase (u50 < 0) and (b) westerly phase (u50 > 0).

RMS Amplitude of SLP Anomalies:

FIG. 9. (a) RMS SLP anomaly amplitudes separated by QBO phases. (b) As in (a), but separated according to combined QBO and ENSO phases. (c),(d) As in Figs. 6b and 6c, but separated by QBO phases. (e),(f) As in (c) and (d), but for more active QBO conditions. (g),(h) As in (c) and (d), but separated according to combined QBO and ENSO phases.

To quantify the similarities/differences between the various MJO phase composites, it is helpful to calculate spatial correlations within the mapped area. The overall correlation coefficient is calculated between all 3° × 3°

grid points on one composite for one MJO phase and the same grid points on a different composite for the same MJO phase. Results for cool ENSO versus warm ENSO and QBOE versus QBOW composites are shown in
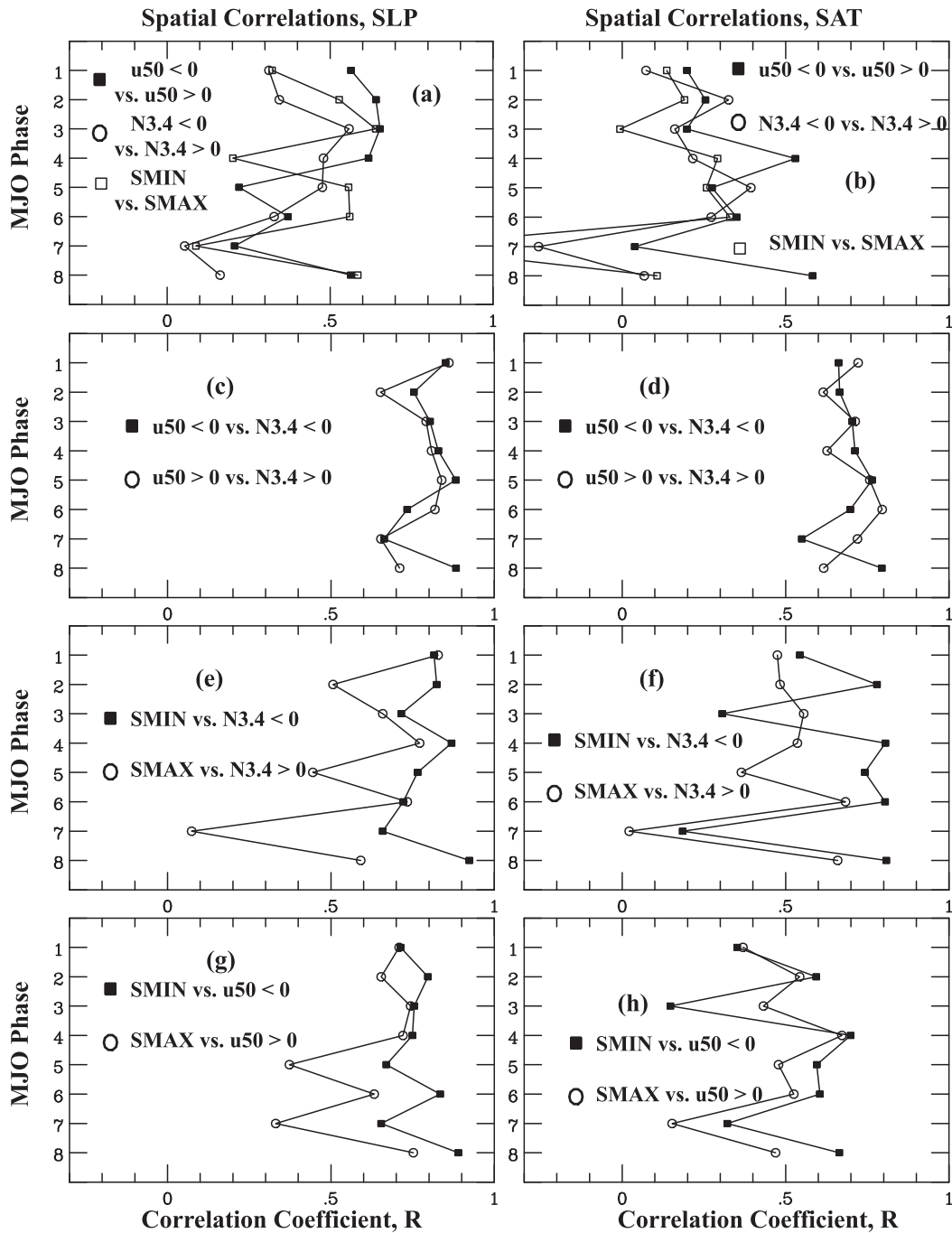
FIG. 10. Spatial correlation coefficients between composited (left) SLP anomalies and (right) SAT anomalies for cool ENSO (N3.4 > 0), easterly QBO (u50 < 0), westerly QBO (u50 > 0), SMIN (F205 < 10.1 mW m^{-2} nm^{-1}), and SMAX (F205 > 10.5 mW m^{-2} nm^{-1}) conditions. Calculations are based on Figs. 4 and 5 (ENSO), Figs. 7 and 8 (QBO), and Figs. S5 and S6 (solar).

Figs. 10a and 10b for the SLP and SAT anomalies, respectively. As expected from the qualitative discussion above, these coefficients are not very high, averaging less than 0.5. Correlations are higher, however, for QBOE versus cool ENSO and QBOW versus warm

ENSO as shown in Figs. 10c and 10d. With the exception of MJO phases 2 and 7, correlation coefficients are generally in the range of 0.7–0.9.

It is unlikely that the similarities between the QBO and ENSO results documented in Figs. 9 and 10 are a

consequence of aliasing of the QBO results by ENSO. Nishimoto and Yoden (2017; see their Fig. 2) have noted a tendency for more strong La Niña events (N3.4 < −1.0) to occur during DJF months under strong QBOE conditions (u50 < −8 m s⁻¹). This potential bias was also noted by Wang et al. (2018a), who tested their results for the QBO influence on the North Pacific storm track by repeating the analysis after discarding winters having significant La Niña events. Results showed that the change in the storm track found during QBOE was not strongly affected by ENSO. During the 1979–2016 NDJFMA months considered here, there were 1058 QBOE days with OMI > 1.5 and 212 of these occurred under cold ENSO conditions (N3.4 < −1 K) whereas only 128 occurred under very warm ENSO conditions (N3.4 > 1 K). So there could be some tendency toward a preferred occurrence of the QBOE phase during cold ENSO conditions. However, the observed strengthening of the QBO influence on the SLP and SAT diagnostics for strong QBO conditions (Figs. 9e,f) supports a real QBO influence. Also, the MJO modulation of the regional SLP and SAT diagnostics is stronger when both easterly QBO and cool ENSO conditions exist than when only cool ENSO conditions exist (cf. Figs. 9g,h with Figs. 6b,c). The latter results are difficult to explain unless the QBO is physically contributing to the forcing of the wave train.

7. Separation by QDO phase

The stratospheric quasi-decadal oscillation (QDO) is an ~11-yr variation of the polar night jet and Brewer–Dobson circulation (BDC) during early boreal winter that is initiated by changes in solar ultraviolet (UV) ozone production and radiative heating in the tropical upper stratosphere (e.g., Haigh 1994; Hood et al. 1993, 2010; Crooks and Gray 2005; Labitzke 2006; Gray et al. 2010). Observational assessments of the QDO are complicated by the shortness of the available data record (about 3.5 solar cycles) and by the lower stratospheric effects of two major volcanic eruptions (El Chichón and Pinatubo), which fortuitously both occurred during declining solar cycle phases in 1982 and 1991, respectively (Chiodo et al. 2014; Kuchar et al. 2017). In addition, the QDO is poorly simulated in most climate models (Mitchell et al. 2015; Hood et al. 2015).

However, the existence of a real QDO is supported by studies on the time scale of the ~27-day solar rotation period, which are statistically more reliable. These studies provide better evidence for stratospheric consequences of solar UV forcing in general (e.g., Hood 1986, 2004; Gruzdev et al. 2009; Garfinkel et al. 2015). Most recently, evidence has been obtained for a reduced occurrence of strong MJO events and increased static stability in the tropical lower stratosphere within a week following peaks in short-term solar UV flux (Hood 2016, 2018). The reverse is found following minima in UV flux.

The available data lead to the expectation that increased UV heating in the tropical upper stratosphere at the maximum phase of the 11-yr solar cycle (SMAX) accelerates the lower mesospheric subtropical jet, modifying planetary wave propagation in such a way as to decelerate the BDC, resulting in relative downwelling and increased static stability in the tropical lower stratosphere (Kodera and Kuroda 2002; Matthes et al. 2004, 2006; Hood 2018). The opposite is expected to occur under solar minimum (SMIN) conditions, leading to relative upwelling, adiabatic cooling, and reduced static stability in the UTLS. These expected characteristics of the QDO are consistent with the results of section 3 (see also Hood 2017), which showed larger occurrence rates of strong MJO events under SMIN conditions as compared to SMAX conditions.

Figures S5 and S6 show compositing results for the two phases of the QDO as defined in section 2 (SMIN and SMAX) in the same format as in Figs. 4 and 5 for ENSO and 7 and 8 for the QBO. Because only strong SMIN and SMAX conditions are considered and since only about 3.5 solar cycles of ERA-Interim reanalysis data are available, the number of qualifying days in each MJO phase composite is more limited than for the ENSO and QBO composites. For example, only 95 days are available in phase 3 for SMAX conditions and the number of degrees of freedom is about 12.

As reviewed above, effects on static stability in the lowermost tropical stratosphere are expected to be in the same direction for SMIN as for QBOE (less stable) and in the same sense for SMAX as for QBOW (more stable). At least in the case of the SMIN results of Figs. S5a and S6a, the calculated evolution of the SLP and SAT anomalies roughly parallels that obtained for QBOE in Figs. 7a and 8a, which is consistent with this expectation. For example, a negative NAO pattern is produced in phases 1 and 2, which leads to a cooling response over eastern North America. A positive NAO pattern is produced by phase 5, leading to a strong warming response in the same region. Cooling anomalies are produced over Eurasia in phases 5 to 7, which is qualitatively consistent with that seen in Fig. 8a. The SLP anomalies over Eurasia evolve from negative values in the early MJO phases to a strong positive anomaly peaking in phase 6, similar to what is shown in Fig. 6a and consistent with a stronger NAO response and farther eastward propagation of the wave train. However, the SMAX results of Figs. S5b and S6b bear only a small resemblance to the QBOW results of Figs. 7b and 8b.

Figure 10 shows spatial correlation results that support the above qualitative comparisons. As seen in Figs. 10e and 10f, spatial correlations between the SMIN and cool ENSO SLP and SAT composites are higher than between the SMAX and warm ENSO composites for nearly all MJO phases. The same is true for spatial correlations between the SMIN and QBOE composites as compared to those between the SMAX and QBOW composites, as shown in Figs. 10g and 10h.

It is unlikely that the poorer agreement of the SMAX results with the cool ENSO and QBOW results is due to aliasing by lower stratospheric heating episodes following the El Chichón and Pinatubo volcanic eruptions. As noted in section 2, the 1982/83 and 1991/92 winters were affected by such heating episodes and fall under SMAX conditions. However, as shown in Fig. S7, excluding these winters from the analysis results in only small changes to the overall evolution of SAT anomalies in Fig. S6b.

Figure 11 shows regional SLP and SAT diagnostic calculations for the two QDO phases in combination with QBO and ENSO phases in a similar format to that of Fig. 6 for ENSO and Fig. 9 for the QBO. As seen in Figs. 11a and 11b, the MJO modulation of these SLP and SAT diagnostics is only marginally stronger during SMIN than during SMAX. The differences are not statistically significant. The same is true for the RMS SLP amplitude diagnostic as shown in Fig. S8a. As seen in Figs. 11c and 11d, the modulation for combined SMIN/ cool ENSO conditions is somewhat stronger than the mean modulation and is also stronger than that obtained for cool ENSO conditions alone (Figs. 6b,c), at least for phases 6 and 1. As seen in Figs. 11e and 11f, the modulation for combined SMIN/QBOE conditions is larger than that obtained for QBOE conditions alone (Figs. 9c,d) for phases 5–7 and 1–2. Figures S9 and S10 show the actual SLP and SAT MJO phase composites for combined SMIN/QBOE and SMAX/QBOW conditions. The MJO modulation of the SLP and SAT anomalies in the North Atlantic/Eurasian sector for this combination of conditions over that for QBOE and QBOW conditions alone appears to be enhanced. The RMS SLP diagnostic for the overall wave train amplitude shows marginally significant enhancements for combined SMIN/QBOE conditions relative to that for SMAX/QBOW conditions only in phases 2 and 6 (Fig. S8b). Finally, as seen in Figs. 11g and 11h, the modulation for combined SMIN/QBOE/cool ENSO conditions is slightly larger still than for SMIN/QBOE conditions during phases 5–6. The actual SLP and SAT MJO phase composites for the SMIN/QBOE/cool ENSO combination are shown in Fig. S11. Results for SMAX/QBOW/warm ENSO conditions are not shown in Figs. 11g and 11h because the number of qualifying

days is too small (averaging 25; less than 10 for several MJO phases) to yield statistically significant results over most of the mapped region.

8. Discussion

The results of this composite analysis provide evidence that the MJO-induced Rossby wave train and its modulation of intraseasonal sea level pressure and surface air temperature anomalies during the extended northern winter season are influenced in similar ways by ENSO, the QBO, and (provisionally) the QDO. Specifically, under cool ENSO, easterly QBO, and SMIN conditions, evidence favors a strengthened wave train that propagates farther eastward and more strongly modulates SLP and SAT anomalies. The modulation is increased further when two or more of these conditions are simultaneously in effect. While internal intraseasonal variability is large and these influences may not be apparent during a given MJO cycle in a given winter, the length of currently available reanalysis datasets allows them to be detected via averaging and construction of mean MJO phase composites.

The SLP and SAT intraseasonal modulations by the MJO occur throughout the northern region considered here, including both the North Pacific and North Atlantic/Eurasian sectors. We have chosen specific diagnostics of these modulations in the North Atlantic/Eurasian sector because they have high amplitudes and are indicative of the strength of the wave train near the end of its propagation path. However, as reviewed in sections 5 and 6, previous work has found evidence in other regions (e.g., the Pacific sector) for an influence of both ENSO and the QBO on MJO-induced intraseasonal climate. Our own preliminary work (not shown here) indicates that the amplitude and areal extent of the North Pacific anticyclonic anomaly are increased in phase 3 under both cool ENSO and QBOE conditions as is the case for the Eurasian anticyclonic anomaly in phases 5 and 6. Further work is needed to verify and extend these results to other northern regions.

We have not attempted to divide the data into winters with and without SSWs. As shown by Schwartz and Garfinkel (2017), there is statistical evidence for an increased occurrence of SSWs following MJO phases 6 and 7, which can lead to a negative NAO-like pattern at the surface, the "troposphere–stratosphere–troposphere" pathway. The latter pathway could be contributing to our compositing results during the earliest MJO phases, in addition to the purely tropospheric Rossby wave train.

Although previous work (e.g., Yoo and Son 2016) and the results of section 3 show that the occurrence rate of strong MJO events (and therefore the mean MJO
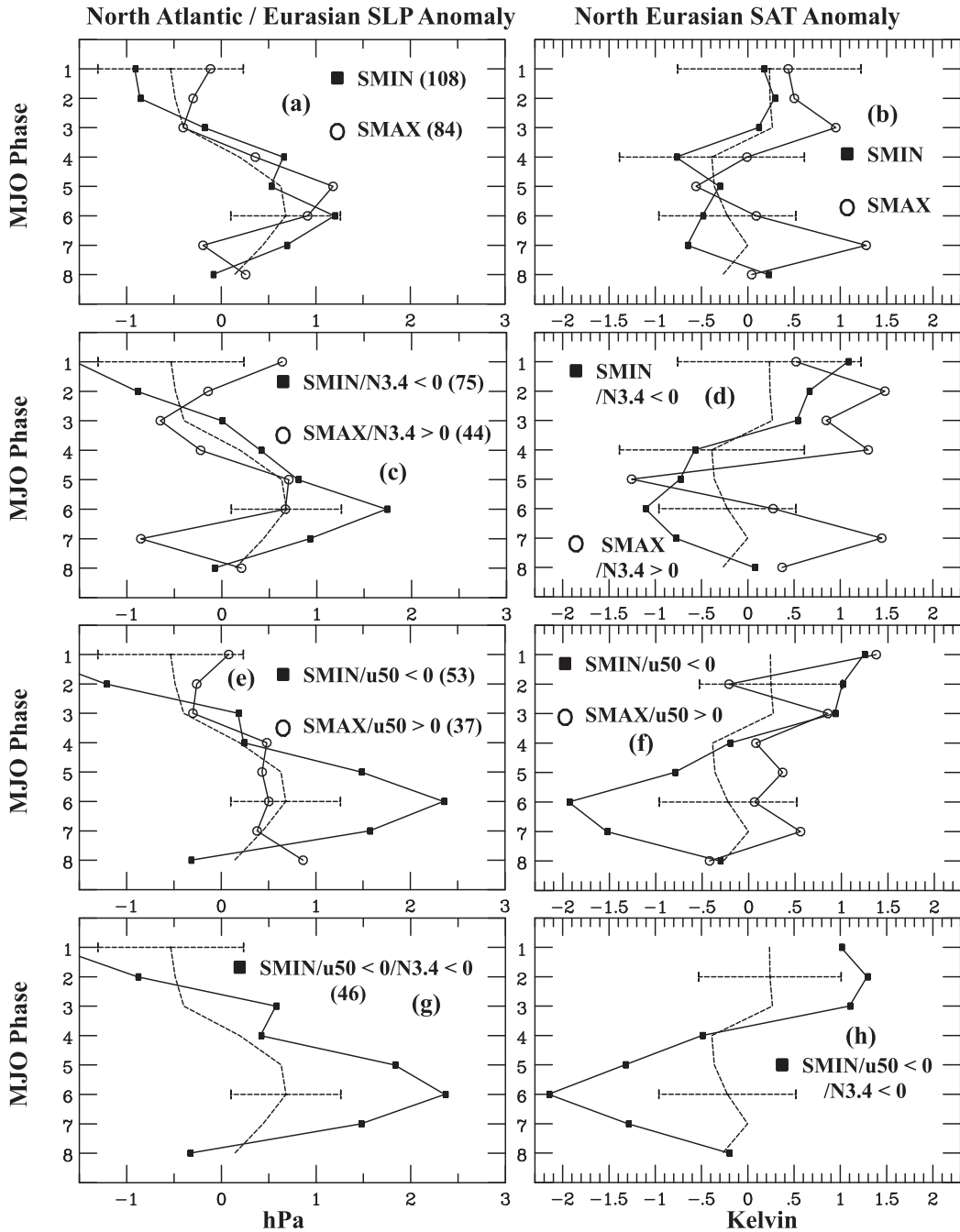
FIG. 11. SLP and SAT diagnostics separated by solar, ENSO, and QBO phases. (a),(b) As in Fig. 6, but for days when the F205 solar index was either <10.1 (SMIN) or >10.5 (SMAX) mW m^{-2} nm^{-1}. (c),(d) As in (a) and (b), but for combined solar and ENSO conditions. (e),(f) As in (a) and (b), but for combined solar and QBO conditions. (g),(h) As in (a) and (b), but for combined SMIN/u50 < 0/N3.4 < 0 conditions.

amplitude) during boreal winter is increased under QBOE and (provisionally) SMIN conditions, it is unlikely that this increased occurrence rate of tropical MJO events alone can explain the evidence presented here for stratospheric influences on the MJO-induced wave train and its extratropical consequences. For example, ENSO has little effect on the overall MJO occurrence rate (Fig. 1) but has a similar effect on the wave train and its modulation of SLP and SAT anomalies, especially for more active ENSO conditions (cf. Figs. 6

and 9). Also, as noted in sections 5 and 6, the mean MJO amplitude for the constructed composites was nearly the same under cool ENSO conditions as under warm ENSO conditions and was only about 6% larger under QBOE conditions than under QBOW conditions. Finally, as discussed in section 6 in relation to Fig. 9, it is unlikely that aliasing from strong ENSO events can explain the evidence for a QBO influence on the wave train and its MJO modulation of intraseasonal SLP and SAT anomalies. Alternate mechanisms by which both ENSO and QBO/solar forcing can similarly affect the overall strength and eastward propagation of the wave train are therefore needed.

As reviewed in section 5, although ENSO has little effect on overall MJO activity, it does influence the longitudinal distribution of this activity such that, during early MJO phases, it is stronger in the Indian Ocean and extends more northward in the warm pool region under La Niña conditions. As shown by Henderson and Maloney (2018), this difference in tropical convective heating distribution may contribute significantly to a stronger extratropical wave source in the subtropical upper tropospheric jet region under La Niña conditions. With respect to the QBO, as mentioned in section 6, observational evidence exists for a slower and more continuous eastward propagation speed of the MJO during boreal winter under QBOE conditions as compared to QBOW conditions. The same is true under cool ENSO conditions as compared to warm ENSO conditions (e.g., Pohl and Matthews 2007). As noted recently by Wang et al. (2018b), according to model experiments reported by Bladé and Hartmann (1995), a slower and more continuous eastward propagation speed may favor development of a stronger extratropical response, including a more well-developed Rossby wave train that could extend farther to the east. This may be consistent with a recent study of fast and slow propagating MJO episodes (Yadav and Straus 2017), which finds that slow episodes produce a stronger enhancement of the positive NAO regime following phase 4 than do fast episodes. Finally, as reviewed in section 7, relative upwelling is expected in the tropical lower stratosphere under SMIN conditions that would reduce static stabilities, thereby favoring increased MJO convection and a stronger Rossby wave source.

But in addition to direct forcing of the wave train amplitude via differences in the convective source distribution and eastward propagation speed of the MJO, it is also possible that differences in the background state zonal wind field (e.g., the seasonally averaged upper tropospheric subtropical jet) are involved in producing the observed differences in the wave train and its extratropical consequences under different tropospheric

and stratospheric conditions. As shown for instance by Henderson and Maloney (2018), the jet is stronger and sharpened in the exit region (i.e., it extends only to the date line) under cool ENSO conditions, which strengthens the Rossby wave source. Garfinkel and Hartmann (2011) have previously found, through both observational analyses and model experiments, that the QBO-induced meridional circulation modifies the midwinter subtropical jet such that it is weakened, especially in the exit region, under QBOE conditions [for a recent summary, see Gray et al. (2018)]. This would also have the effect of modifying the amplitude of the Rossby wave source in that region (Sardeshmukh and Hoskins 1988). With respect to the QDO, observational analyses indicate a strengthening and equatorward shift of the midlatitude jets at SMIN relative to SMAX (Haigh et al. 2005). Using a simplified general circulation model, Simpson et al. (2009, 2010) showed that enhanced heating in the tropical lower stratosphere at SMAX can alter the upward propagation and convergence of planetary-scale Rossby waves in such a way as to explain, at least qualitatively, the observed perturbation of the tropospheric zonal wind field. Although not yet investigated, it is possible that this altered zonal wind structure could also modify the Rossby wave source in the exit region.

While the observational record is too short to confirm the QDO on the 11-yr time scale, supporting evidence for its operation exists on the 27-day time scale (Hood 2016, 2018). As shown by the spatial correlation results of Fig. 10 and the SLP/SAT diagnostic results of Fig. 11, composites for combined SMIN/cool ENSO, SMIN/QBOE, and SMIN/QBOE/cool ENSO conditions produce progressively stronger MJO modulations of mean SLP and SAT anomalies in the North Atlantic/Eurasian sector. These results are consistent with previous work showing that the QBO interacts with other low-frequency stratospheric signals such as the 11-yr solar cycle [see section 4.4 of the review by Baldwin et al. (2001)]. There is no statistically significant relationship between the ENSO and solar cycle (e.g., Haam and Tung 2012). But the influences of both the QBO and the QDO on the MJO-induced wave train may be enhanced under cool ENSO conditions.

anonymous reviewers and the editor, Darryn Waugh, for providing valuable criticisms that improved both the analysis and the presentation.

REFERENCES

Baggett, C. F., E. A. Barnes, E. D. Maloney, and B. D. Mundhenk, 2017: Advancing atmospheric river forecasts into subseasonal-to-seasonal time scales. *Geophys. Res. Lett.*, **44**, 7528–7536, https://doi.org/10.1002/2017GL074434.

Baldwin, M. P., and T. J. Dunkerton, 2001: Stratospheric harbingers of anomalous weather regimes. *Science*, **294**, 581–584, https://doi.org/10.1126/science.1063315.

——, and Coauthors, 2001: The quasi-biennial oscillation. *Rev. Geophys.*, **39**, 179–229, https://doi.org/10.1029/1999RG000073.

Bladé, I., and D. L. Hartmann, 1995: The linear and nonlinear extratropical response of the atmosphere to tropical intraseasonal heating. *J. Atmos. Sci.*, **52**, 4448–4471, https://doi.org/10.1175/1520-0469(1995)052<4448:TLANER>2.0.CO;2.

Bond, N. A., and G. A. Vecchi, 2003: The influence of the Madden–Julian oscillation on precipitation in Oregon and Washington. *Wea. Forecasting*, **18**, 600–613, https://doi.org/10.1175/1520-0434(2003)018<0600:TIOTMO>2.0.CO;2.

Bretherton, C. S., M. Widmann, V. P. Dymnikov, J. M. Wallace, and I. Bladé, 1999: The effective number of spatial degrees of freedom of a time-varying field. *J. Climate*, **12**, 1990–2009, https://doi.org/10.1175/1520-0442(1999)012<1990:TENOSD>2.0.CO;2.

Butler, A., and Coauthors, 2018: Stratosphere–troposphere coupling processes on S2S and longer timescales. *SPARC 2018 General Assembly*, Kyoto, Japan, WCRP, Abstract 1259, www.mete.kugi.kyoto-u.ac.jp/SPARC_GA2018.

Cassou, C., 2008: Intraseasonal interaction between the Madden–Julian oscillation and the North Atlantic oscillation. *Nature*, **455**, 523–527, https://doi.org/10.1038/nature07286.

Chiodo, G., D. R. Marsh, R. Garcia-Herrera, N. Calvo, and J. Garcia, 2014: On the detection of the solar signal in the tropical stratosphere. *Atmos. Chem. Phys.*, **14**, 5251–5269, https://doi.org/10.5194/acp-14-5251-2014.

Collimore, C. C., D. W. Martin, M. H. Hitchman, A. Huesmann, and D. E. Waliser, 2003: On the relationship between the QBO and tropical deep convection. *J. Climate*, **16**, 2552–2568, https://doi.org/10.1175/1520-0442(2003)016<2552:OTRBTQ>2.0.CO;2.

Crooks, A., and L. J. Gray, 2005: Characterization of the 11-year solar signal using a multiple regression analysis of the ERA-40 dataset. *J. Climate*, **18**, 996–1015, https://doi.org/10.1175/JCLI-3308.1.

Dee, D. P., and Coauthors, 2011: The ERA-Interim reanalysis: Configuration and performance of the data assimilation system. *Quart. J. Roy. Meteor. Soc.*, **137**, 553–597, https://doi.org/10.1002/qj.828.

Duchon, C. E., 1979: Lanczos filtering in one and two dimensions. *J. Appl. Meteor.*, **18**, 1016–1022, https://doi.org/10.1175/1520-0450(1979)018<1016:LFIOAT>2.0.CO;2.

Emanuel, K., S. Solomon, D. Folini, S. Davis, and C. Cagnazzo, 2013: Influence of tropical tropopause layer cooling on Atlantic hurricane activity. *J. Climate*, **26**, 2288–2301, https://doi.org/10.1175/JCLI-D-12-00242.1.

Ferranti, L., T. N. Palmer, F. Molteni, and E. Klinker, 1990: Tropical–extratropical interaction associated with the 30–60 day oscillation and its impact on medium and extended range prediction. *J. Atmos. Sci.*, **47**, 2177–2199, https://doi.org/10.1175/1520-0469(1990)047<2177:TEIAWT>2.0.CO;2.

Garfinkel, C. I., and D. L. Hartmann, 2011: The influence of the quasi-biennial oscillation on the troposphere in winter in a

hierarchy of models. Part I: Simplified dry GCMs. *J. Atmos. Sci.*, **68**, 1273–1289, https://doi.org/10.1175/2011JAS3665.1.

——, S. B. Feldstein, D. W. Waugh, C. Yoo, and S. Lee, 2012: Observed connection between stratospheric sudden warmings and the Madden–Julian Oscillation. *Geophys. Res. Lett.*, **39**, L18807, https://doi.org/10.1029/2012GL053144.

——, J. J. Benedict, and E. D. Maloney, 2014: Impact of the MJO on the boreal winter extratropical circulation. *Geophys. Res. Lett.*, **41**, 6055–6062, https://doi.org/10.1002/2014GL061094.

——, V. Silverman, N. Harnik, C. Haspel, and Y. Riz, 2015: Stratospheric response to intraseasonal changes in incoming solar radiation. *J. Geophys. Res. Atmos.*, **120**, 7648–7660, https://doi.org/10.1002/2015JD023244.

Giorgetta, M. A., L. Bengtsson, and K. Arpe, 1999: An investigation of QBO signals in the East Asian and Indian monsoon in GCM experiments. *Climate Dyn.*, **15**, 435–450, https://doi.org/10.1007/s003820050292.

Gray, L. J., and Coauthors, 2010: Solar influences on climate. *Rev. Geophys.*, **48**, RG4001, https://doi.org/10.1029/2009RG000282.

——, J. A. Anstey, Y. Kawatani, H. Lu, S. Osprey, and V. Schenzinger, 2018: Surface impacts of the quasi-biennial oscillation. *Atmos. Chem. Phys.*, **18**, 8227–8247, https://doi.org/10.5194/acp-18-8227-2018.

Gruzdev, A., H. Schmidt, and G. P. Brasseur, 2009: The effect of the solar rotational irradiance variation on the middle and upper atmosphere calculated by a three-dimensional chemistry–climate model. *Atmos. Chem. Phys.*, **9**, 595–614, https://doi.org/10.5194/acp-9-595-2009.

Guo, Y., T. Shinoda, J. Lin, and E. Chang, 2017: Variations of Northern Hemisphere storm track and extratropical cyclone activity associated with the Madden–Julian oscillation. *J. Climate*, **30**, 4799–4818, https://doi.org/10.1175/JCLI-D-16-0513.1.

Haam, E., and K.-K. Tung, 2012: Statistics of solar cycle–La Niña connection: Correlation of two autocorrelated time series. *J. Atmos. Sci.*, **69**, 2934–2939, https://doi.org/10.1175/JAS-D-12-0101.1.

Haigh, J. D., 1994: The role of stratospheric ozone in modulating the solar radiative forcing of climate. *Nature*, **370**, 544–546, https://doi.org/10.1038/370544a0.

——, M. Blackburn, and R. Day, 2005: The response of tropospheric circulation to perturbations in lower-stratospheric temperature. *J. Climate*, **18**, 3672–3685, https://doi.org/10.1175/JCLI3472.1.

Hamill, T. M., and G. N. Kiladis, 2014: Skill of the MJO and Northern Hemisphere blocking in GEFS and medium-range forecasts. *Mon. Wea. Rev.*, **142**, 868–885, https://doi.org/10.1175/MWR-D-13-00199.1.

Henderson, S. A., and E. D. Maloney, 2018: The impact of the Madden–Julian oscillation on high-latitude winter blocking during El Niño–Southern Oscillation events. *J. Climate*, **31**, 5293–5318, https://doi.org/10.1175/JCLI-D-17-0721.1.

——, ——, and E. A. Barnes, 2016: The influence of the Madden–Julian oscillation on Northern Hemisphere winter blocking. *J. Climate*, **29**, 4597–4616, https://doi.org/10.1175/JCLI-D-15-0502.1.

Hendon, H., M. Wheeler, and C. Zhang, 2007: Seasonal dependence of the MJO–ENSO relationship. *J. Climate*, **20**, 531–543, https://doi.org/10.1175/JCLI4003.1.

Hood, L. L., 1986: Coupled stratospheric ozone and temperature responses to short-term changes in solar ultraviolet flux: An analysis of Nimbus 7 SBUV and SAMS data. *J. Geophys. Res.*, **91**, 5264–5276, https://doi.org/10.1029/JD091iD04p05264.

——, 2004: Effects of solar UV variability on the stratosphere. *Solar Variability and Its Effect on Climate, Geophys. Monogr.*, Vol. **141**, Amer. Geophys. Union, 283–304.

——, 2016: Lagged response of tropical tropospheric temperature to solar ultraviolet variations on intraseasonal time scales. *Geophys. Res. Lett.*, **43**, 4066–4075, https://doi.org/10.1002/2016GL068855.

——, 2017: QBO/solar modulation of the boreal winter Madden–Julian oscillation: A prediction for the coming solar minimum. *Geophys. Res. Lett.*, **44**, 3849–3857, https://doi.org/10.1002/2017GL072832.

——, 2018: Short-term solar modulation of the Madden–Julian climate oscillation. *J. Atmos. Sci.*, **75**, 857–873, https://doi.org/10.1175/JAS-D-17-0265.1.

——, J. L. Jirikowic, and J. P. McCormack, 1993: The stratospheric quasi-decadal variation: Influence of long-term solar ultraviolet variations. *J. Atmos. Sci.*, **50**, 3941–3958, https://doi.org/10.1175/1520-0469(1993)050<3941:QDVOTS>2.0.CO;2.

——, B. E. Soukharev, and J. P. McCormack, 2010: Decadal variability of the tropical stratosphere: Secondary influence of the El Niño–Southern Oscillation. *J. Geophys. Res.*, **115**, D11113, https://doi.org/10.1029/2009JD012291.

——, and Coauthors, 2015: Solar signals in CMIP-5 simulations: The ozone response. *Quart. J. Roy. Meteor. Soc.*, **141**, 2670–2689, https://doi.org/10.1002/qj.2553.

Jin, F., and B. J. Hoskins, 1995: The direct response to tropical heating in a baroclinic atmosphere. *J. Atmos. Sci.*, **52**, 307–319, https://doi.org/10.1175/1520-0469(1995)052<0307:TDRTTH>2.0.CO;2.

Kiladis, G. N., J. Dias, K. H. Straub, M. C. Wheeler, S. N. Tulich, K. Kikuchi, K. M. Weickmann, and M. J. Ventrice, 2014: A comparison of OLR and circulation-based indices for tracking the MJO. *Mon. Wea. Rev.*, **142**, 1697–1715, https://doi.org/10.1175/MWR-D-13-00301.1.

Kodera, K., and Y. Kuroda, 2002: Dynamical response to the solar cycle: Winter stratopause and lower stratosphere. *J. Geophys. Res.*, **107**, 4749, https://doi.org/10.1029/2002JD002224.

——, H. Mukougawa, and S. Noguchi, 2018: Role of downward propagating planetary waves in European severe cold snap during a recovery phase of the SSW in February 2018. *SPARC 2018 General Assembly*, Kyoto, Japan, WCRP, Abstract 1202, www-mete.kugi.kyoto-u.ac.jp/SPARC_GA2018.

Kuchar, A., W. Ball, E. Rozanov, A. Stenke, L. Revell, J. Miksovsky, P. Pisoft, and T. Peter, 2017: On the aliasing of the solar cycle in the lower-stratospheric tropical temperature. *J. Geophys. Res. Atmos.*, **122**, 9076–9093, https://doi.org/10.1002/2017JD026948.

Labitzke, K., 2006: Solar variation and stratospheric response. *Space Sci. Rev.*, **125**, 247–260, https://doi.org/10.1007/s11214-006-9061-6.

Lean, J., 2000: A decadal solar effect in the evolution of the Sun's spectral irradiance since the Maunder Minimum. *Geophys. Res. Lett.*, **27**, 2425–2428, https://doi.org/10.1029/2000GL000043.

Lee, R. W., S. Woolnough, A. J. Charlton-Perez, and F. Vitart, 2018: ENSO modulation of MJO teleconnection to the North Atlantic & Europe and implications for subseasonal predictability. *SPARC 2018 General Assembly*, Kyoto, Japan, WCRP, Abstract 1072, www-mete.kugi.kyoto-u.ac.jp/SPARC_GA2018.

Liess, S., and M. A. Geller, 2012: On the relationship between QBO and distribution of tropical deep convection. *J. Geophys. Res.*, **117**, D03108, https://doi.org/10.1029/2011JD016317.

Lin, H., G. Brunet, and J. Derome, 2009: An observed connection between the North Atlantic Oscillation and the Madden–Julian oscillation. *J. Climate*, **22**, 364–380, https://doi.org/10.1175/2008JCLI2515.1.

Liu, C., B. Tian, K.-F. Li, G. L. Manney, N. J. Livesey, Y. L. Yung, and D. E. Waliser, 2014: Northern Hemisphere mid-winter vortex-displacement and vortex-split stratospheric sudden warmings: Influence of the Madden–Julian oscillation and quasi-biennial oscillation. *J. Geophys. Res. Atmos.*, **119**, 12 599–12 620, https://doi.org/10.1002/2014JD021876.

Madden, R. A., and P. R. Julian, 1971: Detection of a 40–50 day oscillation in the zonal wind in the tropical Pacific. *J. Atmos. Sci.*, **28**, 702–708, https://doi.org/10.1175/1520-0469(1971)028<0702:DOADOI>2.0.CO;2.

——, and ——, 1972: Description of global-scale circulation cells in the tropics with a 40–50 day period. *J. Atmos. Sci.*, **29**, 1109–1123, https://doi.org/10.1175/1520-0469(1972)029<1109:DOGSCC>2.0.CO;2.

Matthes, K., U. Langematz, L. L. Gray, K. Kodera, and K. Labitzke, 2004: Improved 11-year solar signal in the Freie Universität Berlin Climate Middle Atmosphere Model (FUB-CMAM). *J. Geophys. Res.*, **109**, D06101, https://doi.org/10.1029/2003JD004012.

——, Y. Kuroda, K. Kodera, and U. Langematz, 2006: Transfer of the solar signal from the stratosphere to the troposphere: Northern winter. *J. Geophys. Res.*, **111**, D06108, https://doi.org/10.1029/2005JD006283.

Matthews, A. J., B. J. Hoskins, and M. Masutani, 2004: The global response to tropical heating in the Madden–Julian oscillation during the northern winter. *Quart. J. Roy. Meteor. Soc.*, **130**, 1991–2011, https://doi.org/10.1256/qj.02.123.

Mitchell, D. M., and Coauthors, 2015: Solar signals in CMIP-5 simulations: The stratospheric pathway. *Quart. J. Roy. Meteor. Soc.*, **141**, 2390–2403, https://doi.org/10.1002/qj.2530.

Moon, J.-Y., B. Wang, and K.-J. Ha, 2011: ENSO regulation of MJO teleconnection. *Climate Dyn.*, **37**, 1133–1149, https://doi.org/10.1007/s00382-010-0902-3.

Nie, J., and A. H. Sobel, 2015: Responses of tropical deep convection to the QBO: Cloud-resolving simulations. *J. Atmos. Sci.*, **72**, 3625–3638, https://doi.org/10.1175/JAS-D-15-0035.1.

Nishimoto, E., and S. Yoden, 2017: Influence of the stratospheric quasi-biennial oscillation on the Madden-Julian oscillation during austral summer. *J. Atmos. Sci.*, **74**, 1105–1125, https://doi.org/10.1175/JAS-D-16-0205.1.

Pawson, S., L. Andrews, L. Coy, R. Cullather, Y. K. Lim, and A. Molod, 2018: The stratospheric warming of 2018 in context of the Earth system. *SPARC 2018 General Assembly*, Kyoto, Japan, WCRP, Abstract 1537, www-mete.kugi.kyoto-u.ac.jp/SPARC_GA2018.

Peristykh, A. N., and P. E. Damon, 2003: Persistence of the Gleissberg 88-year solar cycle over the last ~12,000 years: Evidence from cosmogenic isotopes. *J. Geophys. Res.*, **108**, 1003, https://doi.org/10.1029/2002JA009390.

Plumb, R. A., and R. C. Bell, 1982: A model of the quasi-biennial oscillation on an equatorial beta-plane. *Quart. J. Roy. Meteor. Soc.*, **108**, 335–352, https://doi.org/10.1002/qj.49710845604.

Pohl, B., and A. J. Matthews, 2007: Observed changes in the lifetime and amplitude of the Madden-Julian oscillation associated with the interannual ENSO sea surface temperature anomalies. *J. Climate*, **20**, 2659–2674, https://doi.org/10.1175/JCLI4230.1.

Polvani, L. M., and D. W. Waugh, 2004: Upward wave activity flux as a precursor to extreme stratospheric events and subsequent anomalous surface weather regimes. *J. Climate*, **17**, 3548–3554, https://doi.org/10.1175/1520-0442(2004)017<3548:UWAFAA>2.0.CO;2.

Roundy, P. E., K. MacRitchie, J. Asuma, and T. Melino, 2010: Modulation of the global atmospheric circulation by combined activity in the Madden–Julian oscillation and the El Niño–Southern Oscillation during boreal winter. *J. Climate*, **23**, 4045–4059, https://doi.org/10.1175/2010JCLI3446.1.

Sardeshmukh, P. D., and B. J. Hoskins, 1988: The generation of global rotational flow by steady idealized tropical divergence. *J. Atmos. Sci.*, **45**, 1228–1251, https://doi.org/10.1175/1520-0469(1988)045<1228:TGOGRF>2.0.CO;2.

Scaife, A. A., and Coauthors, 2017: Tropical rainfall, Rossby waves and regional winter climate predictions. *Quart. J. Roy. Meteor. Soc.*, **143**, 1–11, https://doi.org/10.1002/qj.2910.

Schwartz, C., and C. I. Garfinkel, 2017: Relative roles of the MJO and stratospheric variability in North Atlantic and European winter climate. *J. Geophys. Res.*, **122**, 4184–4201, https://doi.org/10.1002/2016JD025829.

Seo, K.-H., H.-J. Lee, and D. M. W. Frierson, 2016: Unraveling the teleconnection mechanisms that induce wintertime temperature anomalies over the Northern Hemisphere continents in response to the MJO. *J. Atmos. Sci.*, **73**, 3557–3571, https://doi.org/10.1175/JAS-D-16-0036.1.

Simpson, I. R., M. Blackburn, and J. D. Haigh, 2009: The role of eddies in driving the tropospheric response to stratospheric heating perturbations. *J. Atmos. Sci.*, **66**, 1347–1365, https://doi.org/10.1175/2008JAS2758.1.

——, ——, ——, and S. Sparrow, 2010: The impact of the state of the troposphere on the response to stratospheric heating in a simplified GCM. *J. Climate*, **23**, 6166–6185, https://doi.org/10.1175/2010JCLI3792.1.

Son, S.-W., Y. Lim, C. Yoo, H. Hendon, and J. Kim, 2017: Stratospheric control of the Madden-Julian oscillation. *J. Climate*, **30**, 1909–1922, https://doi.org/10.1175/JCLI-D-16-0620.1.

Stan, C., D. M. Straus, J. S. Frederiksen, H. Lin, E. D. Maloney, and C. Schumacher, 2017: Review of tropical–extratropical teleconnections on intraseasonal time scales. *Rev. Geophys.*, **55**, 902–937, https://doi.org/10.1002/2016RG000538.

Student, 1908: The probable error of a mean. *Biometrika*, **6**, 1–25.

Takahashi, C., and R. Shirooka, 2014: Storm track activity over the North Pacific associated with the Madden–Julian oscillation under ENSO conditions during boreal winter. *J. Geophys. Res. Atmos.*, **119**, 10 663–10 683, https://doi.org/10.1002/2014JD021973.

Tam, C.-Y., and N.-C. Lau, 2005: The impact of ENSO on atmospheric intraseasonal variability as inferred from observations and GCM simulations. *J. Climate*, **18**, 1902–1924, https://doi.org/10.1175/JCLI3399.1.

Vecchi, G. A., and N. A. Bond, 2004: The Madden–Julian Oscillation (MJO) and northern high latitude wintertime surface air temperatures. *Geophys. Res. Lett.*, **31**, L04104, https://doi.org/10.1029/2003GL018645.

Wallace, J. M., and D. S. Gutzler, 1981: Teleconnections in the geopotential height field during the Northern Hemisphere winter. *Mon. Wea. Rev.*, **109**, 784–812, https://doi.org/10.1175/1520-0493(1981)109<0784:TITGHF>2.0.CO;2.

Wang, J., H.-M. Kim, and E. K. M. Chang, 2018a: Interannual modulation of Northern Hemisphere winter storm tracks by the QBO. *Geophys. Res. Lett.*, **45**, 2786–2794, https://doi.org/10.1002/2017GL076929.

——, ——, ——, and S.-W. Son, 2018b: Modulation of the MJO and North Pacific storm track relationship by the QBO. *J. Geophys. Res.*, **123**, 3976–3990, https://doi.org/10.1029/2017JD027977.

Wheeler, M. C., and H. H. Hendon, 2004: An all-season real-time multivariate MJO index: Development of an index for monitoring and prediction. *Mon. Wea. Rev.*, **132**, 1917–1932, https://doi.org/10.1175/1520-0493(2004)132<1917:AARMMI>2.0.CO;2.

Yadav, P., and D. M. Straus, 2017: Circulation response to fast and slow MJO episodes. *Mon. Wea. Rev.*, **145**, 1577–1596, https://doi.org/10.1175/MWR-D-16-0352.1.

Yoo, C., and S.-W. Son, 2016: Modulation of the boreal wintertime Madden–Julian oscillation by the stratospheric quasi-biennial oscillation. *Geophys. Res. Lett.*, **43**, 1392–1398, https://doi.org/10.1002/2016GL067762.

——, S. Lee, and S. B. Feldstein, 2012: Mechanisms of Arctic surface air temperature change in response to the Madden–Julian oscillation. *J. Climate*, **25**, 5777–5790, https://doi.org/10.1175/JCLI-D-11-00566.1.

Zhang, C., 2013: Madden–Julian oscillation: Bridging weather and climate. *Bull. Amer. Meteor. Soc.*, **94**, 1849–1870, https://doi.org/10.1175/BAMS-D-12-00026.1.

——, and B. Zhang, 2018: QBO–MJO connection. *J. Geophys. Res. Atmos.*, **123**, 2957–2967, https://doi.org/10.1002/2017JD028171.

Zhou, S., M. L'Heureux, S. Weaver, and A. Kumar, 2012: A composite study of the MJO influence on the surface air temperature and precipitation over the continental United States. *Climate Dyn.*, **38**, 1459–1471, https://doi.org/10.1007/s00382-011-1001-9.